Available online at www.sciencedirect.com
SCIENCE DIRECT®
ELSEVIER
European Journal of Mechanics A/Solids 22 (2003) 193–216

A set-valued force law for spatial Coulomb–Contensou friction

R.I. Leine, Ch. Glocker

Institute of Mechanical Systems, Center of Mechanics, ETH Zentrum, CH-8092 Zürich, Switzerland

Received 7 January 2003; accepted 5 February 2003

Abstract

The aim of this paper is to develop a set-valued contact law for combined spatial Coulomb–Contensou friction, taking into account a normal friction torque (drilling friction) and spin. The set-valued Coulomb–Contensou friction law is derived from a non-smooth velocity pseudo potential. A higher-order Runge–Kutta time-stepping method is presented for the numerical simulation of rigid bodies with Coulomb–Contensou friction. The algebraic inclusion describing the contact problem is solved with an Augmented Lagrangian approach. The theory and numerical methods are applied to the Tippe-Top. The analysis and numerical results on the Tippe-Top illustrate the importance of Coulomb–Contensou friction for the dynamics of systems with friction.

Keywords: Contact; Friction; Time-stepping method; Tippe-Top

1. Introduction

The aim of this paper is to develop a contact law for combined spatial Coulomb friction and normal friction torque (drilling friction) as a function of sliding velocity and spin. We will call this extended contact law the Coulomb–Contensou friction law. Coulomb's friction law was formulated as a set-valued force law by Moreau (1988) within a framework of convex analysis. The formulation of frictional contact problems of mechanical rigid multi-body systems with set-valued contact laws leads to a nonlinear algebraic inclusion, which is complicated to solve. The first (and often worst) method is to regularize the set-valued force laws and obtain a stiff problem with an inexact solution. Instead, one simply has to accept the set-valued nature of the problem and deal with the nonlinear algebraic equation. For planar frictional contact problems and for frictionless spatial problems, the contact problem can conveniently be formulated as a Linear Complementarity Problem (Murty, 1988). A linear complementarity formulation for planar rigid-body systems with Coulomb friction was presented in Glocker (1995) and applied to many practical problems (Leine et al., 2003; Pfeiffer and Glocker, 1996; Stiegelmeyr, 2001). Spatial frictional contact can be formulated as a Nonlinear Complementarity Problem (Glocker, 1998, 2001; Stiegelmeyr, 2001), but this has a number of drawbacks. First of all, the numerical solution of the resulting type of NCPs is cumbersome. Secondly, the formulation of spatial anisotropic Coulomb friction or more elaborate friction models such as Coulomb–Contensou friction is complicated and not suitable from a practical point of view. The present study formulates the contact problem for Coulomb–Contensou friction by means of a non-smooth velocity pseudo potential and presents a time-stepping method and an Augmented Lagrangian method for the numerical simulation of rigid bodies with Coulomb–Contensou friction.

The set-valued force law for spatial Coulomb friction describes the friction force $\boldsymbol{\lambda}_T$ of a single contact point with two components $\boldsymbol{\lambda}_T = [\,\lambda_{T1} \quad \lambda_{T2}\,]^{\mathrm{T}}$. The friction force $\boldsymbol{\lambda}_T$ lies within a disk $\|\boldsymbol{\lambda}_T\| \leqslant \mu\lambda_N$ on the tangent plane of the contact point, where μ is the friction coefficient and λ_N is the normal force. The friction disk constitutes a friction cone in the $(\lambda_{T1}, \lambda_{T2}, \lambda_N)$ space. The pair of contacting bodies are assumed to be rigid and impenetrable within the framework of rigid

E-mail addresses: remco.leine@imes.mavt.ethz.ch (R.I. Leine), christoph.glocker@imes.mavt.ethz.ch (Ch. Glocker).

0997-7538/03/$ – see front matter
doi:10.1016/S0997-7538(03)00025-1

multi-body dynamics and the contact is therefore idealized to be a point. The contact point cannot transmit a friction torque and the influence of spin and drilling friction on the sliding friction $\boldsymbol{\lambda}_T$ is therefore usually neglected. In reality, the stiff (but still deformable) bodies deform and touch each other on a small contact surface, being more or less circular. The small deformations of stiff bodies are negligible compared to the geometry of the bodies and the global rigid body motion they undergo, but lead to contacting areas which can influence the dynamics of the system. A contact *surface* cannot only transmit a sliding force $\boldsymbol{\lambda}_T$ tangent to the contact surface, but also transmit a friction torque τ_N normal to the contact surface. The effective radius of the contact surface is influenced by the normal contact force λ_N, the elasticity of the contacting bodies, the surface roughness and the pressure distribution. The friction torque τ_N is, in the absence of sliding and tangential contact force, more or less proportional to the normal contact force, the friction coefficient and the effective radius, i.e., $\tau_N \propto \mu\lambda_N R_{\text{eff}}$. The influence of the friction torque is in most applications neglected because the effective radius is very small in practice. If, however, an object is spinning fastly, then the influence of spin and drilling friction on the dynamics becomes large and can no longer be neglected.

Contensou (1963) realized that drilling friction and especially spin are important for the dynamics of fastly spinning tops. The drilling friction is obviously necessary to describe the gradual loss of energy of the top which brings it back to rest. More of interest is the influence of the spinning velocity on the sliding friction force. A fastly spinning top experiences very little resistance in sliding direction and easily wanders over the floor. The same phenomenon occurs in an electric polishing machine with turning brushes used to clean floors (Magnus, 1971). The machine is hard to move when the brushes are non-rotating (Coulomb friction) but the machine can easily be pushed over the floor with rotating brushes. Contensou (1963) calculated the dependence of the sliding friction force on the sliding velocity v and spin ω, and showed that the sliding friction force vanishes when the ratio $v/(\omega R)$ tends to zero. Furthermore, a stability analysis of a fastly spinning Fleuriais top (a marine navigation instrument) was presented in Contensou (1963). Later, Magnus used Contensou's friction law to give an extensive study of the stability of the Tippe-Top (Magnus, 1971) (see also Kuypers, 1990). Contensou's friction law and the stability of the Tippe-Top were again studied by Friedl (1997), who also gave a Taylor series approximation of the dependence of the sliding friction force on the sliding velocity and spin. In Contensou's original work (Contensou, 1963) the friction force was expressed in elliptic integrals. Zhuravlev (1998) realized that the friction force for a parabolic pressure distribution can be conveniently expressed in elementary functions if the integrals are evaluated in other coordinates. The elliptic integrals cannot be simplified to elementary functions if a uniform pressure distribution is assumed.

In this paper we will formulate Contensou's spatial friction law in the framework of potential theory and subdifferentials, much like the treatment of spatial Coulomb friction in Glocker (2001). We will set-up a non-smooth velocity pseudo potential and approximate it by means of Taylor series for a uniform pressure distribution (like has been done in Friedl, 1997) and subsequently derive the velocity pseudo potential for a parabolic pressure distribution expressed in elementary functions. The friction force and friction torque, as a function of sliding velocity and spin, can then be obtained by taking the subdifferential of the velocity pseudo potential. Subsequently, the dependence of the maximal friction torque on the friction force (and vice versa) will be studied during sticking (no sliding + no spin). A tangential contact torque $\boldsymbol{\tau}_T$ (rolling friction) can arise if the normal pressure distribution is non-symmetrical, but will not be taken into account in the present study. A time-stepping method, based on an Augmented Lagrangian approach, will be presented for the numerical time-integration of systems with Coulomb–Contensou friction. Finally, the theory and numerical methods are applied to the Tippe-Top. The analysis and numerical results on the Tippe-Top illustrate the importance of Coulomb–Contensou friction for the dynamics of systems with friction.

2. Uniform pressure distribution

The friction force and torque are influenced by the distribution of the normal pressure over the contact surface. The pressure distribution depends on the geometry and elasticity properties of the contacting bodies. Local deformations and stresses are not modelled within a rigid multi-body approach. A pressure distribution has therefore to be assumed or to be estimated with analytical methods from the undeformed geometry of the contacting bodies. Contact between locally spherical bodies (e.g., two billiard balls) produces a parabolic pressure distribution according to the law of Hertz (under the assumption of small elastic deformations and frictionless surfaces). Contact between locally flat bodies (e.g., the pressure disks of a clutch) produces a more or less uniform pressure distribution in the interior of the contact surface. A purely uniform pressure distribution cannot exist because the pressure falls to zero at the boundary of the contact surface. A pressure distribution in a practical situation will neither be purely parabolic nor be uniform. Still, the pressure distribution can often well be modelled by a parabolic or a uniform distribution, depending on the geometry of the contacting bodies. A set-valued contact law for a contact surface with a uniform pressure distribution will be derived in this section, and for a parabolic pressure distribution in Section 3.

The coordinate system and geometry of the contact surface are defined in Subsection 2.1 and a non-smooth velocity pseudo potential for a uniform pressure distribution is derived in Subsection 2.2. The force law is subsequently derived from the velocity pseudo potential in Subsection 2.3.

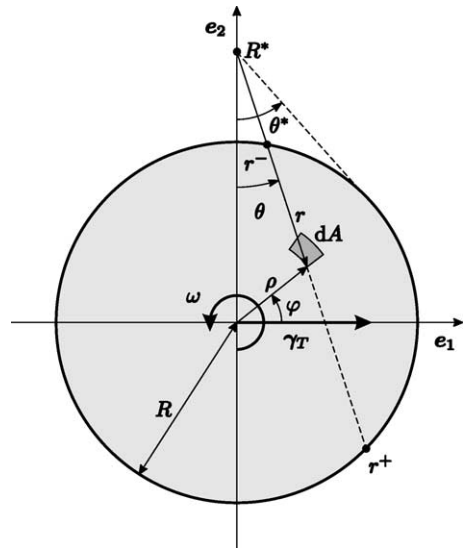

Fig. 1. Coordinates at the contact surface.

2.1. The contact surface

Consider a contact surface (see Fig. 1), which is assumed to be circular with radius R. The relative sliding velocity of the contact is denoted by $\boldsymbol{\gamma}_T$ and the spin by $\boldsymbol{\omega}$. We introduce an orthonormal coordinate frame $(\boldsymbol{e}_1, \boldsymbol{e}_2, \boldsymbol{e}_3)$, of which $\boldsymbol{e}_1$ and $\boldsymbol{e}_2$ span the contact tangent plane and $\boldsymbol{e}_3$ is the unit normal vector on the tangent plane. Without loss of generality we assume that $\boldsymbol{e}_1$ is located such that $\boldsymbol{\gamma}_T = v\boldsymbol{e}_1$. The sliding velocity is therefore expressed by the scalar value v, where $|v| = \|\boldsymbol{\gamma}_T\|$. The spin $\boldsymbol{\omega}$ is normal to the contact plane $\boldsymbol{\omega} = \omega\boldsymbol{e}_3$, i.e., $|\omega| = \|\boldsymbol{\omega}\|$. A surface element $\mathrm{d}A$, at a distance ρ from the origin and an angle φ from the $\boldsymbol{e}_1$ axis, has a sliding velocity of $\boldsymbol{w} = (v - \omega\rho\sin\varphi)\boldsymbol{e}_1 + (\omega\rho\cos\varphi)\boldsymbol{e}_2$. A normal force $\sigma\ \mathrm{d}A$ is acting at the surface element. The normal contact force between the contacting bodies is $\lambda_N = \iint \sigma\ \mathrm{d}A$.

2.2. Velocity potential with uniform pressure distribution

In this subsection we will derive a velocity pseudo potential, which serves as dissipation function for a contact surface with a uniform pressure distribution. The velocity pseudo potential is dependent on the normal contact force, which is in turn dependent on the motion of the system. The velocity *pseudo* potential is therefore not a true potential. In the sequel, the word 'pseudo' will be omitted for brevity. Coulomb's law is assumed to hold on an arbitrary surface element $\mathrm{d}A$ with sliding velocity $\boldsymbol{w}$. The magnitude of the friction force on $\mathrm{d}A$ is according to Coulomb's law $\mathrm{d}\boldsymbol{\lambda}_T = \mu\sigma\ \mathrm{d}A\boldsymbol{w}/\|\boldsymbol{w}\|$. The velocity potential (or dissipation function) for $\mathrm{d}A$ is $\mathrm{d}\Phi = \boldsymbol{w}^{\mathrm{T}}\ \mathrm{d}\boldsymbol{\lambda}_T = \mu\sigma\|\boldsymbol{w}\|\ \mathrm{d}A$. The velocity potential for the total contact surface is obtained by integrating over the contact surface

$$\Phi(\boldsymbol{w}, \sigma) = \iint_A \mu\sigma\|\boldsymbol{w}\|\ \mathrm{d}A. \tag{2.1}$$

Substituting the normal stress for a uniform pressure distribution $\sigma = \lambda_N/A$ in (2.1) and making use of the coordinate system (ρ, φ) gives the double integral

$$\Phi(v, \omega, \lambda_N) = \frac{\mu\lambda_N}{\pi R^2}\int_0^R\int_0^{2\pi} \rho\sqrt{v^2 + (\omega\rho)^2 - 2\omega\rho v\sin\varphi}\ \mathrm{d}\varphi\ \mathrm{d}\rho. \tag{2.2}$$

We introduce the auxiliary variables α and β and the critical radius R^*

$$\alpha = \frac{v}{\omega\rho}, \qquad \beta = \frac{1}{\alpha} = \frac{\omega\rho}{v}, \qquad R^* = \left|\frac{v}{\omega}\right|. \tag{2.3}$$

If $R^* < R$ then the velocity potential (2.2) can be expressed by

$$\Phi(v,\omega,\lambda_N) = \frac{\mu\lambda_N}{\pi R^2}\left(\int_{R^*}^{R}\int_{0}^{2\pi} |\omega|\rho^2\sqrt{\alpha^2+1-2\alpha\sin\varphi}\,\mathrm{d}\varphi\,\mathrm{d}\rho + \int_{0}^{R^*}\int_{0}^{2\pi} |v|\rho\sqrt{\beta^2+1-2\beta\sin\varphi}\,\mathrm{d}\varphi\,\mathrm{d}\rho\right), \tag{2.4}$$

for which holds that $\alpha < 1$ in the first integral and $\alpha > 1$, i.e., $\beta < 1$, in the second integral. The square root terms in the integrands can therefore be approximated by Taylor series

$$\int_0^{2\pi}\sqrt{x^2+1-2x\sin\varphi}\,\mathrm{d}\varphi = \pi\left(2+\frac{1}{2}x^2+\frac{1}{32}x^4+\frac{1}{128}x^6\right)+\mathrm{O}\big(x^8\big), \quad x<1. \tag{2.5}$$

Using (2.5), the potential Φ (2.4) can be approximated by

$$\begin{aligned}
\Phi(v,\omega,\lambda_N) \approx{}& \frac{\mu\lambda_N}{R^2}\left(\int_{R^*}^{R}|\omega|\rho^2\left(2+\frac{1}{2}\alpha^2+\frac{1}{32}\alpha^4+\frac{1}{128}\alpha^6\right)\mathrm{d}\rho + \int_0^{R^*}|v|\rho\left(2+\frac{1}{2}\beta^2+\frac{1}{32}\beta^4+\frac{1}{128}\beta^6\right)\mathrm{d}\rho\right)\\
={}& \frac{\mu\lambda_N}{R^2}\left(\int_{R^*}^{R}|\omega|\left(2\rho^2+\frac{1}{2}\frac{v^2}{\omega^2}+\frac{1}{32}\frac{v^4}{\omega^4}\frac{1}{\rho^2}+\frac{1}{128}\frac{v^6}{\omega^6}\frac{1}{\rho^4}\right)\mathrm{d}\rho\right.\\
&\left.+\int_0^{R^*}|v|\left(2\rho+\frac{1}{2}\frac{\omega^2}{v^2}\rho^3+\frac{1}{32}\frac{\omega^4}{v^4}\rho^5+\frac{1}{128}\frac{\omega^6}{v^6}\rho^7\right)\mathrm{d}\rho\right)\\
={}& \frac{\mu\lambda_N}{R^2}\left(|\omega|\left[\frac{2}{3}\rho^3+\frac{1}{2}\frac{v^2}{\omega^2}\rho-\frac{1}{32}\frac{v^4}{\omega^4}\frac{1}{\rho}-\frac{1}{384}\frac{v^6}{\omega^6}\frac{1}{\rho^3}\right]_{R^*}^{R}\right.\\
&\left.+|v|\left[\rho^2+\frac{1}{8}\frac{\omega^2}{v^2}\rho^4+\frac{1}{192}\frac{\omega^4}{v^4}\rho^6+\frac{1}{1024}\frac{\omega^6}{v^6}\rho^8\right]_0^{R^*}\right)\\
={}& \mu\lambda_N|\omega|R\left(\frac{2}{3}+\frac{1}{2}\frac{v^2}{(\omega R)^2}-\frac{1}{32}\frac{v^4}{(\omega R)^4}-\frac{1}{384}\frac{v^6}{(\omega R)^6}\right)-\underbrace{\mu\lambda_N\frac{5}{3072}\frac{v^3}{(\omega R)^2}}_{\downarrow 0}.
\end{aligned} \tag{2.6}$$

The last term, outside the brackets, is caused by the fact that the two double integrals in (2.4) do not match at $\rho = R^*$ due to the truncation of the Taylor series. This small term tends to zero if (2.5) is approximated with more terms and will be neglected in the sequel. The velocity potential Φ for $R^* > R$, i.e., $|v| > |\omega|R$, is expressed by

$$\Phi(v,\omega,\lambda_N) = \frac{\mu\lambda_N}{\pi R^2}\int_0^{R}\int_0^{2\pi}|v|\rho\sqrt{\beta^2+1-2\beta\sin\varphi}\,\mathrm{d}\varphi\,\mathrm{d}\rho, \tag{2.7}$$

for which holds that $\alpha > 1$, i.e., $\beta < 1$, within the integrand. An approximation for Φ with $R^* > R$ can be found in a similar fashion, which results in the velocity potential for arbitrary values of R^*

$$\Phi(v,\omega,\lambda_N) = \begin{cases} \mu\lambda_N|\omega|R\left(\dfrac{2}{3}+\dfrac{1}{2}u^2-\dfrac{1}{32}u^4-\dfrac{1}{384}u^6+\mathrm{O}\big(u^8\big)\right), & u\leqslant 1,\\[2ex] \mu\lambda_N|\omega|R\left(u+\dfrac{1}{8}\dfrac{1}{u}+\dfrac{1}{192}\dfrac{1}{u^3}+\dfrac{1}{1024}\dfrac{1}{u^5}+\mathrm{O}\left(\dfrac{1}{u^7}\right)\right), & u>1, \end{cases} \tag{2.8}$$

or

$$\Phi(v,\omega,\lambda_N) = \begin{cases} \mu\lambda_N|v|\left(\dfrac{2}{3}\dfrac{1}{u}+\dfrac{1}{2}u-\dfrac{1}{32}u^3-\dfrac{1}{384}u^5+\mathrm{O}\big(u^7\big)\right), & u\leqslant 1,\\[2ex] \mu\lambda_N|v|\left(1+\dfrac{1}{8}\dfrac{1}{u^2}+\dfrac{1}{192}\dfrac{1}{u^4}+\dfrac{1}{1024}\dfrac{1}{u^6}+\mathrm{O}\left(\dfrac{1}{u^8}\right)\right), & u>1, \end{cases} \tag{2.9}$$

where $u = |v|/(|\omega|R) = R^*/R$. Apparently, the velocity potentials for the purely sliding and purely rotating case are

$$\Phi_{\omega=0} = \mu\lambda_N|v| = \mu\lambda_N\|\boldsymbol{\gamma}_T\|, \qquad \Phi_{v=0} = \frac{2}{3}\mu\lambda_N|\omega|R, \tag{2.10}$$

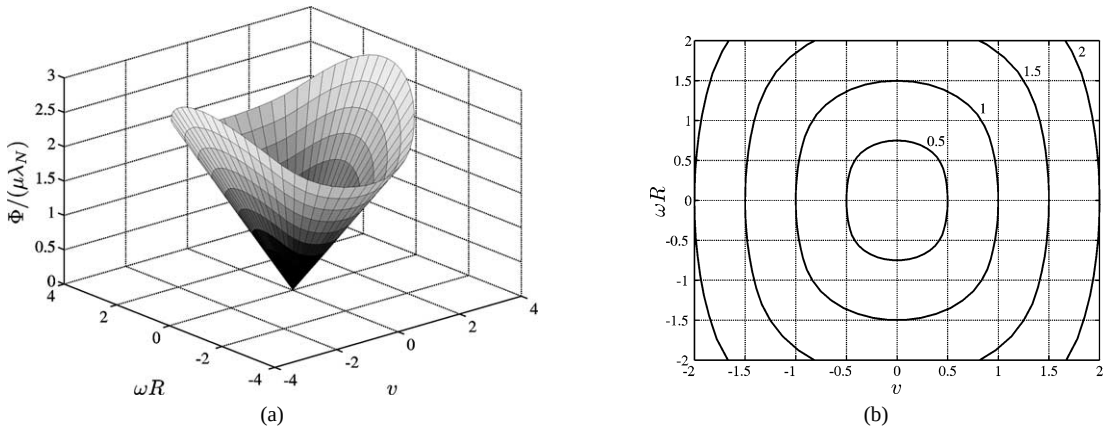

Fig. 2. The velocity potential Φ as function of v and ωR. (a) Cone of the velocity potential. (b) Contour lines of $\Phi/(\mu\lambda_N)$.

which are both non-smooth convex potentials. The velocity potential Φ forms a cone as function of v and ωR, which shown in Fig. 2. The contour lines of the cone are a form between an ellipse and a rectangle.

2.3. Contact laws for a uniform pressure distribution

The tangential friction $\boldsymbol{\lambda}_T$ and the friction torque τ_N can be derived from the velocity potential (2.8) (see Glocker, 2001) via the subdifferential

$$-\boldsymbol{\lambda}_T \in \partial_{\boldsymbol{\gamma}_T}\Phi, \qquad -\tau_N \in \partial_\omega \Phi, \tag{2.11}$$

or, by the chain rule

$$-\boldsymbol{\lambda}_T \in \partial_{\boldsymbol{\gamma}_T}\|\boldsymbol{\gamma}_T\|\,\nabla_{|v|}\Phi, \qquad -\tau_N \in \partial_\omega|\omega|\,\nabla_{|\omega|}\Phi. \tag{2.12}$$

Note that the velocity potential is a smooth function of $|v|$ and $|\omega|$. The force laws are set-valued at $(v,\omega R)=\mathbf{0}$. Using (2.8) and (2.9), we can approximate the force laws with Taylor series

$$-\boldsymbol{\lambda}_T \in \begin{cases} \partial_{\boldsymbol{\gamma}_T}\|\boldsymbol{\gamma}_T\|\mu\lambda_N\left(u-\dfrac{1}{8}u^3-\dfrac{1}{64}u^5+\mathrm{O}(u^7)\right), & u\leqslant 1,\\[2ex] \partial_{\boldsymbol{\gamma}_T}\|\boldsymbol{\gamma}_T\|\mu\lambda_N\left(1-\dfrac{1}{8}\dfrac{1}{u^2}-\dfrac{1}{64}\dfrac{1}{u^4}-\dfrac{5}{1024}\dfrac{1}{u^6}+\mathrm{O}\left(\dfrac{1}{u^8}\right)\right), & u>1, \end{cases} \tag{2.13}$$

$$-\tau_N \in \begin{cases} \partial_\omega|\omega|\mu\lambda_N R\left(\dfrac{2}{3}-\dfrac{1}{2}u^2+\dfrac{3}{32}u^4+\dfrac{5}{384}u^6+\mathrm{O}(u^8)\right), & u\leqslant 1,\\[2ex] \partial_\omega|\omega|\mu\lambda_N R\left(\dfrac{1}{4}\dfrac{1}{u}+\dfrac{1}{48}\dfrac{1}{u^3}+\dfrac{3}{512}\dfrac{1}{u^5}+\mathrm{O}\left(\dfrac{1}{u^7}\right)\right), & u>1. \end{cases} \tag{2.14}$$

Note that the series converge to the same value for $u=1$ because $\frac{2}{3}-\frac{1}{2}+\frac{3}{32}+\frac{5}{384}\approx\frac{1}{4}+\frac{1}{48}+\frac{3}{512}$.

The classical formulation of Coulomb's friction law for spatial contact, without spin and friction torque, states that the set of admissible tangential contact forces is the convex set

$$D_T := \{\boldsymbol{\lambda}_T \mid \|\boldsymbol{\lambda}_T\| \leqslant \mu\lambda_N\}, \tag{2.15}$$

where $D_T(\lambda_N)$ is addressed as the *friction disk* and is a function of the normal force λ_N (Fig. 3). The tangential contact law is for pure Coulomb friction given by

$$-\boldsymbol{\gamma}_T \in N_{D_T}(\boldsymbol{\lambda}_T), \tag{2.16}$$

where $N_{D_T}(\boldsymbol{\lambda}_T)$ is the normal cone to D_T at $\boldsymbol{\lambda}_T$. We will normalize the friction torque τ_N with the constant contact radius R to a force and the angular spin velocity ω to a velocity

$$\lambda_\tau = \frac{\tau_N}{R}, \qquad \gamma_\tau = \omega R. \tag{2.17}$$

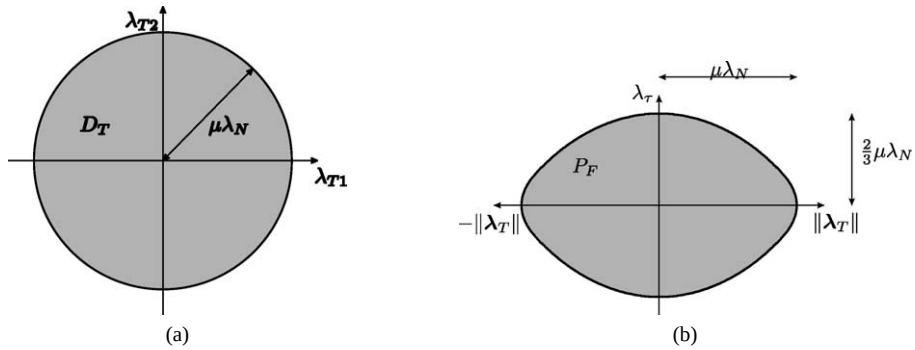

Fig. 3. Admissible tangential forces and normal torque. (a) Friction disk; admissible forces for $\lambda_\tau = 0$. (b) Friction plate; admissible force and torque.

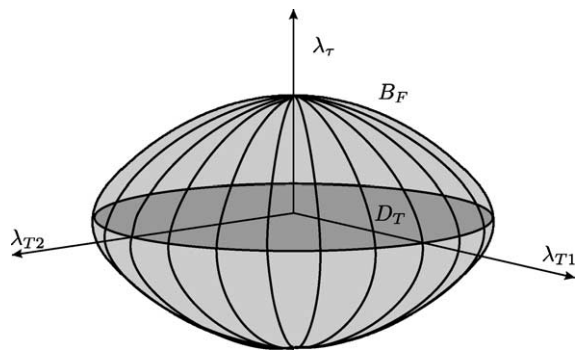

Fig. 4. Friction ball B_F.

We now extend the existing theory for spatial Coulomb friction to spatial Coulomb–Contensou friction taking into account a nonzero friction torque τ_N. The force laws (2.13) and (2.14) give the values of $\boldsymbol{\lambda}_T$ and λ_τ as a function of $\boldsymbol{\gamma}_T$ and γ_τ and implicitly define the set of admissible values of $\boldsymbol{\lambda}_T$ and λ_τ. After eliminating u from (2.13) and (2.14), one can obtain the admissible set $P_F(\lambda_N)$ of $(\|\boldsymbol{\lambda}_T\|, \lambda_\tau)$

$$P_F := \begin{cases} \left\{ \|\boldsymbol{\lambda}_T\|, \lambda_\tau \;\middle|\; \xi = \dfrac{\|\boldsymbol{\lambda}_T\|}{\mu\lambda_N}, \eta = \dfrac{\lambda_\tau}{\mu\lambda_N};\ \dfrac{9}{4}\eta^2 + \dfrac{3}{2}\xi^2 - \dfrac{15}{32}\xi^4 - \dfrac{5}{128}\xi^6 + \mathrm{O}(\xi^8) \leqslant 1 \right\}, & \xi \leqslant \xi^*, \\ \left\{ \|\boldsymbol{\lambda}_T\|, \lambda_\tau \;\middle|\; \xi = \dfrac{\|\boldsymbol{\lambda}_T\|}{\mu\lambda_N}, \eta = \dfrac{\lambda_\tau}{\mu\lambda_N};\ \xi^2 + 4\eta^2 - \dfrac{20}{3}\eta^4 + \dfrac{40}{9}\eta^6 + \mathrm{O}(\eta^8) \leqslant 1 \right\}, & \xi > \xi^*, \end{cases} \tag{2.18}$$

with $\xi^* = 1 - \frac{1}{8} - \frac{1}{64} + \cdots$. We will call $P_F(\lambda_N)$ the *friction plate*. The friction plate P_F is shown in Fig. 3b (the border has been obtained numerically with the series of (2.18)). The admissible set of tangential friction forces and normal friction torque forms a squashed ball $B_F(\lambda_N)$ in the $(\lambda_{T1}, \lambda_{T2}, \lambda_\tau)$ space,

$$B_F := \begin{cases} \left\{ \boldsymbol{\lambda}_T, \lambda_\tau \;\middle|\; \xi = \dfrac{\|\boldsymbol{\lambda}_T\|}{\mu\lambda_N}, \eta = \dfrac{\lambda_\tau}{\mu\lambda_N};\ \dfrac{9}{4}\eta^2 + \dfrac{3}{2}\xi^2 - \dfrac{15}{32}\xi^4 - \dfrac{5}{128}\xi^6 + \mathrm{O}(\xi^8) \leqslant 1 \right\}, & \xi \leqslant \xi^*, \\ \left\{ \boldsymbol{\lambda}_T, \lambda_\tau \;\middle|\; \xi = \dfrac{\|\boldsymbol{\lambda}_T\|}{\mu\lambda_N}, \eta = \dfrac{\lambda_\tau}{\mu\lambda_N};\ \xi^2 + 4\eta^2 - \dfrac{20}{3}\eta^4 + \dfrac{40}{9}\eta^6 + \mathrm{O}(\eta^8) \leqslant 1 \right\}, & \xi > \xi^*. \end{cases} \tag{2.19}$$

The squashed ball B_F (Fig. 4) is axisymmetric around the λ_τ axis. The intersection of B_F with the $(\lambda_{T1}, \lambda_{T2})$ plane is formed by the friction disk D_T. Any intersection of B_F orthogonal to D_T will give the friction plate P_F. The contact law for spatial Coulomb–Contensou friction can now be expressed by means of the friction ball

$$-\boldsymbol{\gamma}_F \in N_{B_F}(\boldsymbol{\lambda}_F), \tag{2.20}$$

with

$$\boldsymbol{\gamma}_F = \begin{bmatrix} \gamma_{T1} \\ \gamma_{T2} \\ \gamma_\tau \end{bmatrix}, \qquad \boldsymbol{\lambda}_F = \begin{bmatrix} \lambda_{T1} \\ \lambda_{T2} \\ \lambda_\tau \end{bmatrix}, \tag{2.21}$$

where $N_{B_F}(\boldsymbol{\lambda}_F)$ is the normal cone to $B_F(\lambda_N)$ at $\boldsymbol{\lambda}_F$.

The magnitude of the friction force $\boldsymbol{\lambda}_T$ as a function of u (2.13) is shown in Fig. 5(a) and the magnitude of λ_τ as a function of $1/u$ (2.14) is shown in Fig. 5(b) (solid lines). The functions both start at the origin and have an asymptote at $\|\boldsymbol{\lambda}_T\| = \mu\lambda_N$ and $|\lambda_\tau| = \frac{2}{3}\mu\lambda_N$ respectively. The friction characteristic $\boldsymbol{\lambda}_T(v)$ for a fixed value of γ_τ can be derived from (2.13) and is shown in Fig. 6(a) for different fixed values of γ_τ. The curves for $\gamma_\tau > 0$ are all single-valued functions of v. Apparently, a superimposed spin ω on a sliding velocity v causes a smoothing effect of the friction characteristic $\boldsymbol{\lambda}_T(v)$. The friction characteristic for $\gamma_\tau = 0$ is (for $\lambda_\tau = 0$) the classical set-valued friction characteristic of Coulomb. Similarly, the dependence of λ_τ on γ_τ, for different fixed values of v, is shown in Fig. 6(b). The same smoothing effect occurs in the $\lambda_\tau(\gamma_\tau)$ relation ship due to a superimposed velocity $v > 0$. Again, a set-valued relationship is obtained for $v = 0$, which corresponds (for $\boldsymbol{\lambda}_T = 0$) to the classical set-valued friction law of a purely rotational contact. The boundaries $\|\boldsymbol{\lambda}_T\| = \mu\lambda_N$ and $|\lambda_\tau| = \frac{2}{3}\mu\lambda_N$ of the sets for $v = \gamma_\tau = 0$ are the extreme values of the friction ball $B_F(\lambda_N)$ along its principal axes. For the classical set-valued friction characteristic of Coulomb (i.e., a purely translational contact $\lambda_\tau = 0$, $\gamma_\tau = 0$), the magnitude friction force $\|\boldsymbol{\lambda}_T\|$ rises up to the value $\mu\lambda_N$ when the contact changes from a sticking state to sliding. This is in general *not* the case for Coulomb–Contensou friction as soon as we have some rotation. A sticking contact obeying Coulomb–Contensou's friction law will start slipping for $\|\boldsymbol{\lambda}_T\| < \mu\lambda_N$ if $\lambda_\tau \neq 0$. The slip-criterion for Coulomb–Contensou friction is given by $(\boldsymbol{\lambda}_T, \lambda_\tau) \in \partial B_F(\lambda_N)$.

The set-valued force law presented in this section is able to describe the smooth characteristic of the friction forces for nonzero slip and spin velocity as well as the set-valued nature of friction forces when the contact sticks ($v = 0$, $\gamma_\tau = 0$). Moreover, the force law provides the correct slip-criterion when both applied forces and torques are present. Coulomb–Contensou's force law reduces to the set-valued Coulomb's law when the contact radius vanishes ($R = 0$).

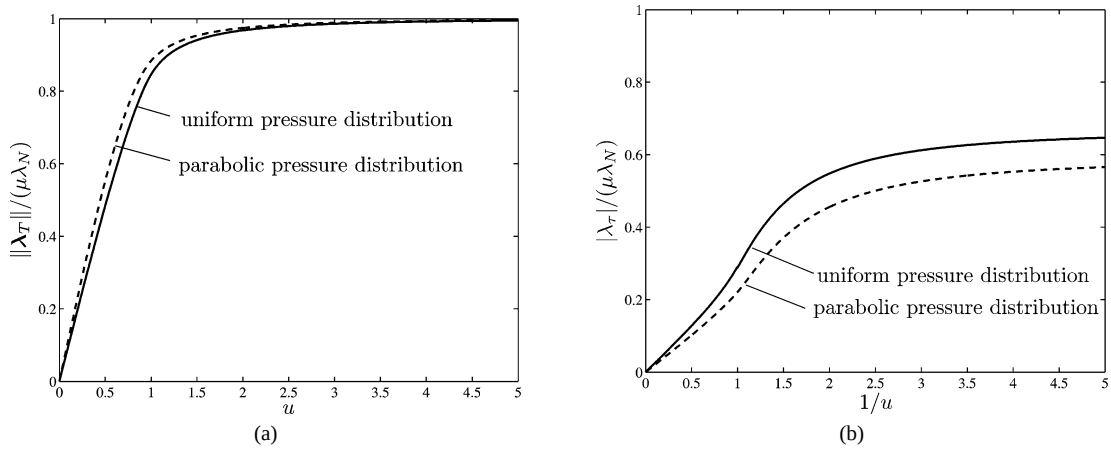

(a) (b)

Fig. 5. Friction force and torque as a function of u for a uniform pressure distribution (solid) and for a parabolic pressure distribution (dashed).

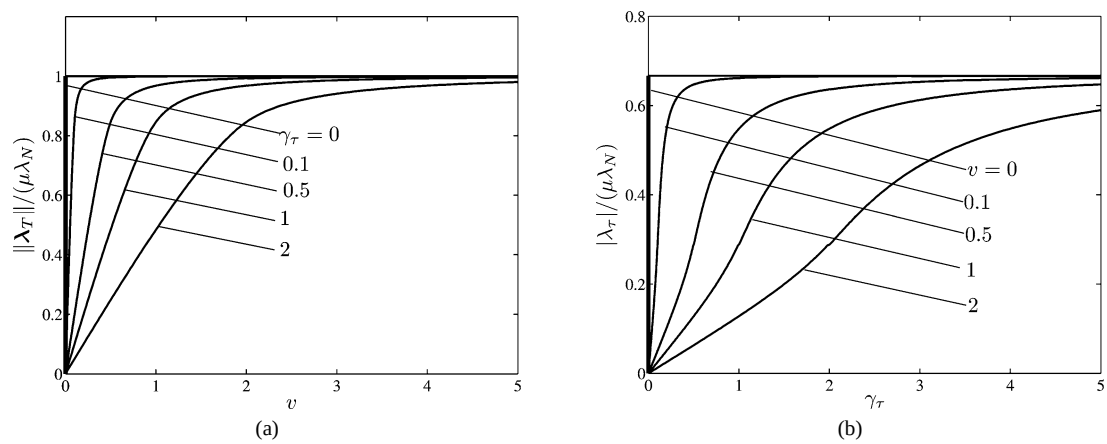

(a) (b)

Fig. 6. Dependence of friction force and normalized torque on γ_τ and v for a uniform pressure distribution. (a) $\boldsymbol{\lambda}_T$ as function of v for fixed values of γ_τ. (b) $\boldsymbol{\lambda}_\tau$ as function of γ_τ for fixed values of v.

3. Parabolic pressure distribution

In this section we will derive the contact laws and velocity potential for a Hertz contact with parabolic pressure distribution and constant contact radius. In the previous section we studied a contact with uniform pressure distribution by means of Taylor series. The velocity potential with a parabolic pressure distribution, however, can be expressed in elementary functions (Zhuravlev, 1998). Hereto, we introduce the coordinates r and θ, which are polar coordinates around the pole $R^*\boldsymbol{e}_2$ (see Fig. 1). The relation between the coordinates (r,θ) and (ρ,φ) is given by

$$\rho\cos\varphi = r\sin\theta, \qquad \rho\sin\varphi + r\cos\theta = R^* = \left|\frac{v}{\omega}\right|. \tag{3.1}$$

We will assume a circular contact surface with radius R. The contact radius R is for a Hertz contact (Johnson, 1985) a function of the normal load λ_N

$$R(\lambda_N) = \left(\frac{3\varrho^*\lambda_N}{4E^*}\right)^{1/3}, \tag{3.2}$$

where $1/\varrho^* = 1/\varrho_1 + 1/\varrho_2$ is the relative curvature and E^* is the effective elasticity modulus

$$\frac{1}{E^*} = \frac{1-\nu_1^2}{E_1} + \frac{1-\nu_2^2}{E_2}, \tag{3.3}$$

with ϱ_i, E_i, ν_i being the radii, elasticity moduli and Poisson constants of the contacting bodies. However, the theoretical contact radius according to Hertz is for relatively hard bodies extremely small. Instead, we will assume that the radius of the contact surface is determined by the surface roughness and meso-scopic non-convexity of the contacting bodies, which is for hard bodies more realistic. The contact radius is therefore assumed to be constant, i.e., $R = R_0$. The Hertz normal pressure distribution is given by the parabolic function

$$\sigma = \frac{3\lambda_N}{2\pi R^2}\sqrt{1-\frac{\rho^2}{R^2}} = \frac{3\lambda_N}{2\pi R^2}\sqrt{-q^2+2qu\cos\theta+1-u^2}, \tag{3.4}$$

with $u = R^*/R$ and $q = r/R$. The magnitude of the velocity $\boldsymbol{w}$ simplifies in (r,θ) coordinates to

$$\|\boldsymbol{w}\| = \sqrt{(v-\omega\rho\sin\varphi)^2 + (\omega\rho\cos\varphi)^2} = |\omega r|. \tag{3.5}$$

3.1. Velocity potential with parabolic pressure distribution

The velocity potential $\Phi(v,\omega,\lambda_N)$ defined by (2.1) is now expressed as a double integral in the coordinates (r,θ)

$$\Phi(v,\omega,\lambda_N) = \begin{cases} \displaystyle\int_0^{\pi}\int_{r^-}^{r^+} \mu\sigma\|\boldsymbol{w}\| r \,\mathrm{d}r\,\mathrm{d}\theta, & u \leqslant 1, \\ \displaystyle 2\int_0^{\theta^*}\int_{r^-}^{r^+} \mu\sigma\|\boldsymbol{w}\| r \,\mathrm{d}r\,\mathrm{d}\theta, & u > 1. \end{cases} \tag{3.6}$$

Substitution of (3.4) in (3.6) and making use of the normalized radius $q = r/R$ gives

$$\Phi(v,\omega,\lambda_N) = \begin{cases} \displaystyle\frac{3\mu\lambda_N}{2\pi R^2}|\omega|\int_0^{\pi}\int_{r^-}^{r^+}\sigma r^2 \,\mathrm{d}r\,\mathrm{d}\theta = \frac{3\mu\lambda_N}{2\pi}R|\omega|\int_0^{\pi} Q_2\,\mathrm{d}\theta, & u \leqslant 1, \\ \displaystyle\frac{3\mu\lambda_N}{\pi R^2}|\omega|\int_0^{\theta^*}\int_{r^-}^{r^+}\sigma r^2 \,\mathrm{d}r\,\mathrm{d}\theta = \frac{3\mu\lambda_N}{\pi}R|\omega|\int_0^{\theta^*} Q_2\,\mathrm{d}\theta, & u > 1, \end{cases} \tag{3.7}$$

with

$$Q_2 = \int_{q^-}^{q^+}\sqrt{-q^2+2qu\cos\theta+1-u^2}\,q^2\,\mathrm{d}q, \tag{3.8}$$

and the integration limits

$$r^{\pm} = r\cos\theta \pm \sqrt{R^{*2} - r^2\sin^2\theta}, \tag{3.9}$$

$$q^{\pm} = u\cos\theta \pm \sqrt{1 - u^2\sin^2\theta}. \tag{3.10}$$

First, the integral $Q_2 = \int_{q^-}^{q^+} q^2\sqrt{aq^2+bq+c}\,\mathrm{d}q$ is evaluated with $a=-1$, $b=2u\cos\theta$, $c=1-u^2$, $\Delta=-4(1-u^2\sin^2\theta)$ by making use of (A.1), (A.2) and (A.3) (see Appendix A)

$$\begin{aligned} Q_2 &= -\frac{5b^2-4ac}{16a^2}\frac{\Delta}{8a}\frac{1}{\sqrt{-a}}\left[\arcsin\left(\frac{2aq+b}{\sqrt{-\Delta}}\right)\right]_{q^-}^{q^+} \\ &= \frac{(5b^2+4c)\Delta}{128}\left[\arcsin\left(\frac{-2q+b}{\sqrt{-\Delta}}\right)\right]_{q^-}^{q^+} \\ &= -\frac{(4u^2-5u^2\sin^2\theta+1)(1-u^2\sin^2\theta)}{8}\left[\arcsin\left(\frac{-q+u\cos\theta}{\sqrt{1-u^2\sin^2\theta}}\right)\right]_{q^-}^{q^+} \\ &= \frac{\pi}{8}\left(5u^4\sin^4\theta - \left(4u^4+6u^2\right)\sin^2\theta + 1 + 4u^2\right). \end{aligned} \tag{3.11}$$

Subsequently, the integral (3.7) can be evaluated using (A.4) and (A.5). For $u \leqslant 1$ we obtain

$$\begin{aligned} \Phi(v,\omega,\lambda_N) &= \frac{3\mu\lambda_N}{16}R|\omega|\int_0^{\pi}\left(5u^4\sin^4\theta - \left(4u^4+6u^2\right)\sin^2\theta + 1 + 4u^2\right)\mathrm{d}\theta \\ &= \frac{3\mu\lambda_N}{16}R|\omega|\pi\left(-\frac{1}{8}u^4 + u^2 + 1\right), \end{aligned} \tag{3.12}$$

and for $u > 1$

$$\begin{aligned} \Phi(v,\omega,\lambda_N) &= \frac{3\mu\lambda_N}{8}R|\omega|\int_0^{\theta^*}\left(5u^4\sin^4\theta - \left(4u^4+6u^2\right)\sin^2\theta + 1 + 4u^2\right)\mathrm{d}\theta \\ &= \frac{3\mu\lambda_N}{8}R|\omega|\left(5u^4\left(\frac{3}{8}\theta^* - \frac{1}{4}\sin 2\theta^* + \frac{1}{32}\sin 4\theta^*\right) - \left(4u^4+6u^2\right)\left(\frac{1}{2}\theta^* - \frac{1}{4}\sin 2\theta^*\right) + \left(1+4u^2\right)\theta^*\right) \\ &= \frac{3\mu\lambda_N}{8}R|\omega|\left(\left(-\frac{1}{8}u^4 + u^2 + 1\right)\theta^* + \left(-\frac{1}{4}u^4 + \frac{3}{2}u^2\right)\sin 2\theta^* + \frac{5}{32}u^4\sin 4\theta^*\right) \\ &= \frac{3\mu\lambda_N}{8}R|\omega|\left(\left(-\frac{1}{8}u^4 + u^2 + 1\right)\theta^* + \left(\frac{1}{8}u^2 + \frac{7}{4}\right)\sqrt{u^2-1}\right), \end{aligned} \tag{3.13}$$

with $\sin\theta^* = 1/u$, $\sin 2\theta^* = (2/u^2)\sqrt{u^2-1}$, $\sin 4\theta^* = (4/u^2)(1-2/u^2)\sqrt{u^2-1}$. Summarizing, the velocity potential for a parabolic pressure distribution reads as

$$\Phi(v,\omega,\lambda_N) = \begin{cases} \dfrac{3\mu\lambda_N}{128}R|\omega|\pi\left(-u^4+8u^2+8\right), & u \leqslant 1, \\ \dfrac{3\mu\lambda_N}{64}R|\omega|\left(\left(-u^4+8u^2+8\right)\arcsin\dfrac{1}{u} + \left(u^2+14\right)\sqrt{u^2-1}\right), & u > 1, \end{cases} \tag{3.14}$$

where $u = u(v,\omega)$ and R is constant.

3.2. Contact laws for a parabolic pressure distribution

The set-valued force laws for Coulomb–Contensou friction with a parabolic pressure distribution can be derived from the velocity potential (3.14) similar to the discussion of the uniform pressure distribution. The friction torque τ_N will again be normalized with the constant contact radius R to a force and the angular spin velocity ω to a velocity

$$\lambda_\tau = \frac{\tau_N}{R}, \qquad \gamma_\tau = \omega R. \tag{3.15}$$

The velocity potential (3.14) can be expressed in terms of $\Phi(v,\omega,\lambda_N)$ as well as in terms of $\Phi(\boldsymbol{\gamma}_T,\gamma_\tau,\lambda_N)$. Using the definitions of the set-valued force laws

$$-\boldsymbol{\lambda}_T \in \partial_{\boldsymbol{\gamma}_T}\|\boldsymbol{\gamma}_T\|\nabla_{|v|}\Phi, \qquad -\lambda_\tau \in \partial_{\gamma_\tau}|\gamma_\tau|\nabla_{|\gamma_\tau|}\Phi \tag{3.16}$$

and the velocity potential (3.14), we can derive the force laws

$$-\boldsymbol{\lambda}_T \in \begin{cases} \partial_{\boldsymbol{\gamma}_T}\|\boldsymbol{\gamma}_T\|\dfrac{3\mu\lambda_N}{32}\pi u\left(-u^2+4\right), & u\leqslant 1,\\ \partial_{\boldsymbol{\gamma}_T}\|\boldsymbol{\gamma}_T\|\dfrac{3\mu\lambda_N}{16}\dfrac{1}{u}\left(u^2\left(4-u^2\right)\arcsin\left(\dfrac{1}{u}\right)+\left(u^2+2\right)\sqrt{u^2-1}\right), & u>1, \end{cases} \tag{3.17}$$

$$-\lambda_\tau \in \begin{cases} \partial_{\gamma_\tau}|\gamma_\tau|\dfrac{3\mu\lambda_N}{128}\pi\left(3u^4-8u^2+8\right), & u\leqslant 1,\\ \partial_{\gamma_\tau}|\gamma_\tau|\dfrac{3\mu\lambda_N}{64}\left(\left(3u^4-8u^2+8\right)\arcsin\left(\dfrac{1}{u}\right)+\left(-3u^2+6\right)\sqrt{u^2-1}\right), & u>1. \end{cases} \tag{3.18}$$

The magnitude of the friction force $\boldsymbol{\lambda}_T$ and as a function of u (3.17) and λ_τ as a function of $1/u$ (3.18) for a parabolic pressure distribution is shown in Fig. 5 (dashed lines). The force laws (3.17) and (3.18) give the values of $\boldsymbol{\lambda}_T$ and λ_τ as a function of $\boldsymbol{\gamma}_T$ and γ_τ and implicitly define the set of admissible values of $\boldsymbol{\lambda}_T$ and λ_τ. The friction plate $P_F(\lambda_N)$, being the admissible set of $(\|\boldsymbol{\lambda}_T\|,\lambda_\tau)$, can be obtained after eliminating u from (3.17) and (3.18)

$$P_F := \begin{cases} \left\{\|\boldsymbol{\lambda}_T\|,\lambda_\tau \;\middle|\; \dfrac{9}{64}\left(\dfrac{\eta}{\eta^*}\right)^2+\dfrac{9}{8}\left(\dfrac{\xi}{\xi^*}\right)^2-\dfrac{243}{1024}\left(\dfrac{\xi}{\xi^*}\right)^4-\dfrac{9}{32768}\left(\dfrac{\xi}{\xi^*}\right)^6+\mathrm{O}\left(\left(\dfrac{\xi}{\xi^*}\right)^8\right)\leqslant 1\right\}, & \xi\leqslant\xi^*,\\ \left\{\|\boldsymbol{\lambda}_T\|,\lambda_\tau \;\middle|\; \xi^2+5\eta^2-\dfrac{75}{7}\eta^4+\dfrac{1250}{147}\eta^6+\mathrm{O}\left(\eta^8\right)\leqslant 1\right\}, & \xi>\xi^*, \end{cases} \tag{3.19}$$

with

$$\xi=\frac{\|\boldsymbol{\lambda}_T\|}{\mu\lambda_N}, \qquad \eta=\frac{\lambda_\tau}{\mu\lambda_N}, \tag{3.20}$$

and $\xi^*=\frac{9}{32}\pi$, $\eta^*=\frac{9}{128}\pi$. The admissible set of tangential friction forces and normal friction torque forms the friction ball $B_F(\lambda_N)$ in the $(\lambda_{T1},\lambda_{T2},\lambda_\tau)$ space,

$$B_F := \begin{cases} \left\{\boldsymbol{\lambda}_T,\lambda_\tau \;\middle|\; \dfrac{9}{64}\left(\dfrac{\eta}{\eta^*}\right)^2+\dfrac{9}{8}\left(\dfrac{\xi}{\xi^*}\right)^2-\dfrac{243}{1024}\left(\dfrac{\xi}{\xi^*}\right)^4-\dfrac{9}{32768}\left(\dfrac{\xi}{\xi^*}\right)^6+\mathrm{O}\left(\left(\dfrac{\xi}{\xi^*}\right)^8\right)\leqslant 1\right\}, & \xi\leqslant\xi^*,\\ \left\{\boldsymbol{\lambda}_T,\lambda_\tau \;\middle|\; \xi^2+5\eta^2-\dfrac{75}{7}\eta^4+\dfrac{1250}{147}\eta^6+\mathrm{O}\left(\eta^8\right)\leqslant 1\right\}, & \xi>\xi^*. \end{cases} \tag{3.21}$$

Similar to the discussion of the uniform pressure distribution, one can express the contact law for spatial Coulomb–Contensou friction with parabolic pressure distribution by means of the friction ball

$$-\boldsymbol{\gamma}_F \in N_{B_F}(\boldsymbol{\lambda}_F), \tag{3.22}$$

with (2.21) where $N_{B_F}(\boldsymbol{\lambda}_F)$ is the normal cone to $B_F(\lambda_N)$ at $\boldsymbol{\lambda}_F$.

The force laws and velocity potential for a parabolic pressure distribution were derived in this section. The force laws for a parabolic pressure distribution appear to be qualitatively similar to the force laws for a uniform pressure distribution and differ maximally about 20 percent in magnitude (see Fig. 5). The friction plate P_F and friction ball B_F for a parabolic pressure distribution (not depicted) are therefore very similar in shape to the sets shown in Figs. 3 and 4.

4. Multibody formulation of systems with Coulomb–Contensou friction

In this section the numerical simulation of multibody system with Coulomb–Contensou friction will be discussed. The main rigid-body integration techniques for systems with unilateral constraints are the event-driven integration method and the time-stepping method (Anitescu and Potra, 1997; Brogliato, 1999; Glocker, 1995, 1998; Moreau, 1988; Pfeiffer and Glocker, 1996; Stewart and Trinkle, 1996; Stiegelmeyr, 2001).

The event-driven integration method uses a standard ODE solver for integration in smooth phases of the motion. The constraints are expressed on acceleration level and integration is stopped when an event occurs. Usually a Linear (or nonlinear) Complementarity Problem is solved to determine the next hybrid mode after the event.

Time-stepping methods are based on using a time-discretization of generalized positions $\boldsymbol{q}$ and velocities $\boldsymbol{u}$, usually with a fixed step-size. Integrals of forces over each time-step are used instead of the instantaneous values of the forces. The time-stepping method makes no distinction between impulsive forces (due to impacts) and finite forces. Only increments of the positions and velocities are computed. The acceleration $\dot{\boldsymbol{u}}$ is not computed by the algorithm, as it becomes infinite for impulsive forces. The positions and velocities at the end of the time-step are found by solving an algebraic inclusion which describes the contact problem (for instance by formulating it as a (Non)linear Complementarity Problem). Multiple events might take place during one time-step, and the algorithm computes the overall integral of the forces over this time-step, which is finite. The time-stepping method is especially useful when one is interested in the global motion of systems with many contact points, leading to a large number of events. Each individual event is for those applications not of importance but the global motion is determined by the sum of all events. The benefit of time-stepping methods over event-driven integration methods is the fact that no (or less) event-detection and index sets are needed. This makes the algorithm less complex, more robust and will give a reduction in computation time when many contacts are involved. A second advantage of the time-stepping method is its capability to pass accumulation points of impacts. A notable disadvantage of the time-stepping method is its low-order accuracy. The time-stepping method was introduced by Moreau (1988) and has been subsequently developed in Anitescu and Potra (1997), Stewart and Trinkle (1996), Stiegelmeyr (2001).

The event-driven integration method and the time-stepping method have been applied to mechanical systems with *Coulomb* friction. In this section we will describe the time-stepping method of Moreau (1988) and combine it with the Augmented Lagrangian Method (Alart and Curnier, 1991; Simo and Laursen, 1992; Laursen and Simo, 1993) in order to solve the *Coulomb–Contensou* contact problem. Furthermore, we will extend the time-stepping method of Moreau to a fourth-order Runge–Kutta time-stepping method. A brief discussion of the Augmented Lagrangian will be given first.

4.1. Augmented Lagrangian Method

The dynamics of a multibody system during an impact free part of the motion can be expressed by the equation of motion on acceleration level (Pfeiffer and Glocker, 1996)

$$\boldsymbol{M}(t,\boldsymbol{q})\dot{\boldsymbol{u}} - \boldsymbol{h}(t,\boldsymbol{q},\boldsymbol{u}) - \boldsymbol{W}_N(t,\boldsymbol{q})\boldsymbol{\lambda}_N - \boldsymbol{W}_F(t,\boldsymbol{q})\boldsymbol{\lambda}_F = \boldsymbol{0}, \tag{4.1}$$

with the set-valued force laws

$$-\boldsymbol{g}_N \in N_{C_N}(\boldsymbol{\lambda}_N), \qquad -\boldsymbol{\gamma}_F \in N_{B_F(\lambda_N)}(\boldsymbol{\lambda}_F), \tag{4.2}$$

where $\boldsymbol{M}$ is the symmetric mass matrix, $\boldsymbol{q}$ the vector with generalized coordinates, $\boldsymbol{u} = \dot{\boldsymbol{q}}$ is the vector with generalized velocities and $\boldsymbol{h}$ is the vector with all smooth elastic, gyroscopic and dissipating generalized forces. The normal contact force of contact i is denoted by λ_{Ni} and the vector of generalized friction forces by $\boldsymbol{\lambda}_{Fi}$. The vectors $\boldsymbol{w}_{Ni}$ and $\boldsymbol{w}_{Fi}$ are the generalized normal and sliding force directions of contact i and constitute the matrices $\boldsymbol{W}_N = \{\boldsymbol{w}_{Ni}\}$ and $\boldsymbol{W}_F = \{\boldsymbol{w}_{Fi}\}$. The dual variables to the normal contact forces $\boldsymbol{\lambda}_N$ are the variations of the normal gap distances $\boldsymbol{g}_N$ and the dual variables to the generalized friction forces $\boldsymbol{\lambda}_F$ are the variations of the generalized sliding velocities $\boldsymbol{\gamma}_F$.

The usual equation of motion, which relates acceleration to forces, is not suited to describe motion with impact. We replace the equation of motion on acceleration level by an equality of measures (Glocker, 2001; Moreau, 1988)

$$\boldsymbol{M}\,\mathrm{d}\boldsymbol{u} - \boldsymbol{h}\,\mathrm{d}t - \boldsymbol{W}_N\,\mathrm{d}\boldsymbol{\Lambda}_N - \boldsymbol{W}_F\,\mathrm{d}\boldsymbol{\Lambda}_F = \boldsymbol{0}, \tag{4.3}$$

or more briefly as

$$\boldsymbol{M}\,\mathrm{d}\boldsymbol{u} - \boldsymbol{h}\,\mathrm{d}t - \boldsymbol{W}\,\mathrm{d}\boldsymbol{\Lambda} = \boldsymbol{0}, \tag{4.4}$$

where the dependence of the system matrices on $t, \boldsymbol{q}$ and $\dot{\boldsymbol{q}}$ has been omitted for brevity. We denote with $\mathrm{d}t$ the Lebesgue-measure and with $\mathrm{d}\eta$ the sum of the dirac pulses at the impact times. The measure for the velocities $\mathrm{d}\boldsymbol{u} = \dot{\boldsymbol{u}}\,\mathrm{d}t + (\boldsymbol{u}^+ - \boldsymbol{u}^-)\,\mathrm{d}\eta$ is split in a Lebesgue-measurable part and an atomic part. The atomic part consists of the left and right limit of $\boldsymbol{u}$ at t. For impact free motion it holds that $\mathrm{d}\boldsymbol{u} = \dot{\boldsymbol{u}}\,\mathrm{d}t$. Similarly, the measure for the impulses is defined as $\mathrm{d}\boldsymbol{\Lambda} = \boldsymbol{\lambda}\,\mathrm{d}t + \boldsymbol{\Lambda}\,\mathrm{d}\eta$.

The constraints on velocity level can be expressed in the left and right limits of $\boldsymbol{u}$

$$\boldsymbol{\gamma}^+ = \boldsymbol{W}^{\mathrm{T}}\boldsymbol{u}^+ + \widetilde{\boldsymbol{w}}, \qquad \boldsymbol{\gamma}^- = \boldsymbol{W}^{\mathrm{T}}\boldsymbol{u}^- + \widetilde{\boldsymbol{w}}. \tag{4.5}$$

For impact free motion it holds that $\boldsymbol{\gamma} = \boldsymbol{\gamma}^+ = \boldsymbol{\gamma}^-$.

At this point we discretize the measure differential equation by integrating over a small but finite time interval Δt

$$\int_{\Delta t} \mathrm{d}\boldsymbol{u} = \Delta\boldsymbol{u}, \qquad \int_{\Delta t} \boldsymbol{h}\,\mathrm{d}t = \Delta\boldsymbol{h} \approx \boldsymbol{h}\Delta t, \qquad \int_{\Delta t} \mathrm{d}\boldsymbol{\Lambda} = \boldsymbol{\Lambda}, \tag{4.6}$$

and we obtain the equation of motion in differences

$$\boldsymbol{M}\Delta\boldsymbol{u} - \boldsymbol{h}\Delta t - \boldsymbol{W}_N\boldsymbol{\Lambda}_N - \boldsymbol{W}_F\boldsymbol{\Lambda}_F = \boldsymbol{0}. \tag{4.7}$$

The force laws for completely inelastic contact with friction can be put in the form

$$-\boldsymbol{\Lambda}_N \in \partial\Psi_{\mathbb{R}^+}\big(\boldsymbol{\gamma}_N^+\big), \qquad -\boldsymbol{\Lambda}_F \in \partial\Phi\big(\boldsymbol{\gamma}_F^+\big), \tag{4.8}$$

where $\Psi_{\mathbb{R}^+}$ is the indicator function of convex analysis on $\mathbb{R}^+$ with

$$\boldsymbol{\gamma}_N^+ = \boldsymbol{W}_N^{\mathrm{T}}(\boldsymbol{u}^- + \Delta\boldsymbol{u}) + \widetilde{\boldsymbol{w}}_N, \qquad \boldsymbol{\gamma}_F^+ = \boldsymbol{W}_F^{\mathrm{T}}(\boldsymbol{u}^- + \Delta\boldsymbol{u}) + \widetilde{\boldsymbol{w}}_F. \tag{4.9}$$

In each incremental step, say time-step, we have to solve $\Delta\boldsymbol{u}$ and $(\boldsymbol{\Lambda}_N, \boldsymbol{\Lambda}_F)$ from the equation of motion (4.7) and the force laws (4.8), which forms a set of algebraic *inclusions*. An elegant way to solve such a set of algebraic inclusions is by transforming the problem to a constrained optimization problem. The constrained optimization problem can subsequently be transformed to an *unconstrained* mini-max problem by making use of the Augmented Lagrangian (Rockafellar, 1976). The solution to the algebraic inclusion then corresponds to a saddle-point of the Augmented Lagrangian.

The (quasi) Augmented Lagrangian for a frictional contact problem can be expressed as (see Alart and Curnier, 1991)

$$\begin{aligned} L_A(\Delta\boldsymbol{u}, \boldsymbol{\Lambda}_N, \boldsymbol{\Lambda}_F) \;=\; & \frac{1}{2}\big\|\Delta\boldsymbol{u} - \boldsymbol{M}^{-1}\boldsymbol{h}\Delta t\big\|_{\boldsymbol{M}}^2 - \boldsymbol{\gamma}_N^{\mathrm{T}}(\Delta\boldsymbol{u})\boldsymbol{\Lambda}_N - \boldsymbol{\gamma}_F^{\mathrm{T}}(\Delta\boldsymbol{u})\boldsymbol{\Lambda}_F \\ & + \frac{r}{2}\big\|\boldsymbol{\gamma}_N(\Delta\boldsymbol{u})\big\|^2 - \frac{1}{2r}\operatorname{dist}_{C_N}^2\big(\boldsymbol{\Lambda}_N - r\boldsymbol{\gamma}_N(\Delta\boldsymbol{u})\big) \\ & + \frac{r}{2}\big\|\boldsymbol{\gamma}_F(\Delta\boldsymbol{u})\big\|^2 - \frac{1}{2r}\operatorname{dist}_{B_F}^2\big(\boldsymbol{\Lambda}_F - r\boldsymbol{\gamma}_F(\Delta\boldsymbol{u})\big), \end{aligned} \tag{4.10}$$

where B_F is dependent on the normal force[1] and $r > 0$. The Augmented Lagrangian L_A is dependent on a parameter $r > 0$, which (loosely speaking) controls the steepness of L_A in the region where the Lagrangian L,

$$L(\Delta\boldsymbol{u}, \boldsymbol{\Lambda}_N, \boldsymbol{\Lambda}_F) = \frac{1}{2}\big\|\Delta\boldsymbol{u} - \boldsymbol{M}^{-1}\boldsymbol{h}\Delta t\big\|_{\boldsymbol{M}}^2 - \boldsymbol{\gamma}_N^{\mathrm{T}}(\Delta\boldsymbol{u})\boldsymbol{\Lambda}_N - \boldsymbol{\gamma}_F^{\mathrm{T}}(\Delta\boldsymbol{u})\boldsymbol{\Lambda}_F, \tag{4.11}$$

is constrained as well as an additional penalty term in the direction $\Delta\boldsymbol{u}$. The value of r should be taken large enough to make the problem well conditioned in the constrained region, but not too high in order to prevent ill-conditioning due to the penalty term $\frac{r}{2}\|\boldsymbol{\gamma}(\Delta\boldsymbol{u})\|^2$.

We will make use of the following properties of distances and proximal points on a convex set C

$$\operatorname{prox}_C(\boldsymbol{x}) = \operatorname*{argmin}_{\forall\boldsymbol{x}^*\in C} \|\boldsymbol{x} - \boldsymbol{x}^*\|, \qquad \operatorname{dist}_C(\boldsymbol{x}) = \big\|\boldsymbol{x} - \operatorname{prox}_C(\boldsymbol{x})\big\|, \tag{4.12}$$

$$\nabla\frac{1}{2}\operatorname{dist}_C^2(\boldsymbol{x}) = \boldsymbol{x} - \operatorname{prox}_C(\boldsymbol{x}), \tag{4.13}$$

$$f(\boldsymbol{x}) = -\boldsymbol{x}^{\mathrm{T}}\boldsymbol{y} + \frac{1}{2}\|\boldsymbol{x}\|^2 - \frac{1}{2}\operatorname{dist}_C^2(\boldsymbol{y} - \boldsymbol{x}) \Longrightarrow \nabla f(\boldsymbol{x}) = -\boldsymbol{y} + \boldsymbol{x} + \big[\boldsymbol{y} - \boldsymbol{x} - \operatorname{prox}_C(\boldsymbol{y} - \boldsymbol{x})\big] = -\operatorname{prox}_C(\boldsymbol{y} - \boldsymbol{x}). \tag{4.14}$$

Evaluating the stationarity conditions of the saddle-point of L_A gives the equations

$$\begin{aligned} &\nabla_{\Delta\boldsymbol{u}} L_A(\Delta\boldsymbol{u}, \boldsymbol{\Lambda}_N, \boldsymbol{\Lambda}_F) = \boldsymbol{M}\Delta\boldsymbol{u} - \boldsymbol{h}\Delta t - \boldsymbol{W}_N\Pi_N(\boldsymbol{\Lambda}_N, \boldsymbol{\gamma}_N) - \boldsymbol{W}_F\Pi_F(\boldsymbol{\Lambda}_N, \boldsymbol{\Lambda}_F, \boldsymbol{\gamma}_F) = \boldsymbol{0}, \\ &\nabla_{\boldsymbol{\Lambda}_N} L_A(\Delta\boldsymbol{u}, \boldsymbol{\Lambda}_N, \boldsymbol{\Lambda}_F) = -\frac{1}{r}\big(\boldsymbol{\Lambda}_N - \Pi_N(\boldsymbol{\Lambda}_N, \boldsymbol{\gamma}_N)\big) = \boldsymbol{0}, \\ &\nabla_{\boldsymbol{\Lambda}_F} L_A(\Delta\boldsymbol{u}, \boldsymbol{\Lambda}_N, \boldsymbol{\Lambda}_F) = -\frac{1}{r}\big(\boldsymbol{\Lambda}_F - \Pi_F(\boldsymbol{\Lambda}_N, \boldsymbol{\Lambda}_F, \boldsymbol{\gamma}_F)\big) = \boldsymbol{0}, \end{aligned} \tag{4.15}$$

where use has been made of (4.12)–(4.14) and the abbreviations

$$\begin{aligned} &\Pi_N(\boldsymbol{\Lambda}_N, \boldsymbol{\gamma}_N) = \operatorname{prox}_{C_N}(\boldsymbol{\Lambda}_N - r\boldsymbol{\gamma}_N), \\ &\Pi_F(\boldsymbol{\Lambda}_N, \boldsymbol{\Lambda}_F, \boldsymbol{\gamma}_F) = \operatorname{prox}_{B_F(\boldsymbol{\Lambda}_N)}(\boldsymbol{\Lambda}_F - r\boldsymbol{\gamma}_F). \end{aligned} \tag{4.16}$$

Note that $\boldsymbol{\gamma}_N = \boldsymbol{\gamma}_N(\Delta\boldsymbol{u})$ and $\boldsymbol{\gamma}_F = \boldsymbol{\gamma}_F(\Delta\boldsymbol{u})$. We therefore obtain the set of algebraic equations

[1] To be more precise, it holds that $B_F = B_F(\operatorname{prox}_{\mathbb{R}^+}(\boldsymbol{\Lambda}_N - r\boldsymbol{\gamma}_N(\Delta\boldsymbol{u}))$, see Alart and Curnier (1991).

$$\begin{aligned}
&\boldsymbol{M}\Delta\boldsymbol{u} - \boldsymbol{h}\Delta t - \boldsymbol{W}_N \Pi_N(\boldsymbol{\Lambda}_N, \boldsymbol{\gamma}_N) - \boldsymbol{W}_F \Pi_F(\boldsymbol{\Lambda}_N, \boldsymbol{\Lambda}_F, \boldsymbol{\gamma}_F) = \boldsymbol{0},\\
&\boldsymbol{\Lambda}_N = \Pi_N(\boldsymbol{\Lambda}_N, \boldsymbol{\gamma}_N),\\
&\boldsymbol{\Lambda}_F = \Pi_F(\boldsymbol{\Lambda}_N, \boldsymbol{\Lambda}_F, \boldsymbol{\gamma}_F).
\end{aligned} \tag{4.17}$$

The saddle point of the Augmented Lagrangian, being the solution to the set of algebraic equations, can be found with a Modified Newton algorithm (Alart and Curnier, 1991). More elaborate methods also exist but we will discuss the Modified Newton Method because of its simplicity.

The Modified Newton Method uses initial guesses for the impulses, $\boldsymbol{\Lambda}_N^k$ and $\boldsymbol{\Lambda}_F^k$ for $k = 1$, and iterates the scheme

1. Solve $\Delta\boldsymbol{u}^{k+1}$ from $\boldsymbol{M}\Delta\boldsymbol{u}^{k+1} = \boldsymbol{h}\Delta t + \boldsymbol{W}_N\boldsymbol{\Lambda}_N^k + \boldsymbol{W}_F\boldsymbol{\Lambda}_F^k$.
2. Project $\boldsymbol{\Lambda}_N^{k+1} = \Pi_N(\boldsymbol{\Lambda}_N^k, \boldsymbol{\gamma}_N^{k+1})$, $\boldsymbol{\Lambda}_F^{k+1} = \Pi_F(\boldsymbol{\Lambda}_N^{k+1}, \boldsymbol{\Lambda}_F^k, \boldsymbol{\gamma}_F^{k+1})$ with $\boldsymbol{\gamma}_N^{k+1} = \boldsymbol{W}_N^{\mathrm{T}}(\Delta\boldsymbol{u}^{k+1} + \boldsymbol{u}^k) + \boldsymbol{w}_N$, $\boldsymbol{\gamma}_F^{k+1} = \boldsymbol{W}_F^{\mathrm{T}}(\Delta\boldsymbol{u}^{k+1} + \boldsymbol{u}^k) + \boldsymbol{w}_F$

until the error $\|\boldsymbol{\Lambda}_N^{k+1} - \boldsymbol{\Lambda}_N^k\| + \|\boldsymbol{\Lambda}_F^{k+1} - \boldsymbol{\Lambda}_F^k\|$ is within some tolerance.

4.2. Time-stepping method

In the sequel of this section we will present time-stepping methods, which use the Augmented Lagrangian Method to solve the contact problem. We first discuss the time-stepping method of Moreau, which is basically a special kind of midpoint DAE solver. Consider the positions $\boldsymbol{q}_A$ and velocities $\boldsymbol{u}_A$ to be known at the beginning of the time-step at time t_A. The algorithm takes first a half time-step for the positions and arrives at the midpoint $\boldsymbol{q}_M = \boldsymbol{q}_A + \frac{1}{2}\Delta t\boldsymbol{u}_A$. The midpoint is used to classify the status of the normal constraints, which allows for an index reduction. The contact set $I_N = \{i \mid g_{Ni}(t_M, \boldsymbol{q}_M) \leqslant 0\}$ is calculated at the midpoint and used to set-up the contact problem on velocity level for both the normal and tangential constraints. The set I_N contains all indices of the closed contact points. A corresponding set I_F is derived from I_N, containing all indices of friction forces which participate in the contact. The velocity $\boldsymbol{u}_E$, at the end of time-step $t_E = t_A + \Delta t$, is subsequently calculated by a trapezoidal scheme

$$\boldsymbol{M}_M(\boldsymbol{u}_E - \boldsymbol{u}_A) = \boldsymbol{h}_M\Delta t + \boldsymbol{W}_{NM}\boldsymbol{\Lambda}_N + \boldsymbol{W}_{FM}\boldsymbol{\Lambda}_F, \tag{4.18}$$

and the set-valued force laws

$$-\boldsymbol{\Lambda}_N \in \partial\Psi_{\mathbb{R}^+}(\boldsymbol{\gamma}_N^+), \qquad -\boldsymbol{\Lambda}_F \in \partial\Phi(\boldsymbol{\gamma}_F^+), \tag{4.19}$$

where $\boldsymbol{M}_M$, $\boldsymbol{h}_M$, $\boldsymbol{W}_{NM}$ and $\boldsymbol{W}_{FM}$ are the system matrices evaluated at the midpoint. This set of algebraic inclusions can be solved using an Augmented Lagrangian approach together with a Modified Newton Method. Finally, the positions at the end of the time-step are calculated $\boldsymbol{q}_E = \boldsymbol{q}_M + \frac{1}{2}\Delta t\boldsymbol{u}_E$. The algorithm is summarized in Table 1, which shows how the Augmented Lagrangian Method is combined with the time-stepping method. The algorithm is implemented such that the calculated impulses $\boldsymbol{\Lambda}_N$ and $\boldsymbol{\Lambda}_F$ are used as initial guesses for the Augmented Lagrangian calculation in the next time-step.

The time-stepping method of Moreau is very elegant due to its simplicity but suffers from the fact that it is at best a second-order method. Mechanical systems can exhibit high frequency oscillations during smooth parts of the motion, which require a higher-order integration scheme. We will present a four-stage Runge–Kutta method based on the time-stepping method of Moreau. The four-stage Runge–Kutta method achieves a fourth-order accuracy during smooth parts of the motion and first-order accuracy if an impact is encountered during the time-step. The basic construction scheme of a Runge–Kutta method for a differential equation $\dot{x} = f(t, x)$ is

$$\begin{aligned}
&X_1 = x_n,\\
&X_i = x_n + \Delta t\sum_{j=1}^{i-1} a_{ij} f(t_n + c_j\Delta t, X_j), \quad i = 2, \ldots, s,\\
&x_{n+1} = x_n + \Delta t\sum_{i=1}^{s} b_i f(t_n + c_i\Delta t, X_i)
\end{aligned} \tag{4.20}$$

Table 1
Moreau's time-stepping method with an Augmented Lagrangian approach

function $[t, \boldsymbol{q}, \boldsymbol{u}] = \mathit{TimeSteppingMethodMoreau}(t_0, t_{\text{end}}, \boldsymbol{q}_0, \boldsymbol{u}_0, N, \text{tol})$

$\Delta t = \frac{t_{\text{end}} - t_0}{N-1}$ Initialize

$t^1 = t_0, \quad \boldsymbol{q}^1 = \boldsymbol{q}_0, \quad \boldsymbol{u}^1 = \boldsymbol{u}_0$

$\boldsymbol{\Lambda}_N = \boldsymbol{0}, \quad \boldsymbol{\Lambda}_F = \boldsymbol{0}$

for $j = 1$ **to** N Do all time-steps

$t_A = t^j, \quad \boldsymbol{q}_A = \boldsymbol{q}^j, \quad \boldsymbol{u}_A = \boldsymbol{u}^j$

$t_M = t_A + \frac{1}{2}\Delta t, \quad \boldsymbol{q}_M = \boldsymbol{q}_A + \frac{1}{2}\Delta t \boldsymbol{u}_A$ Do half a time-step

$\boldsymbol{M}_M = \boldsymbol{M}(t_M, \boldsymbol{q}_M), \quad \boldsymbol{h}_M = \boldsymbol{h}(t_M, \boldsymbol{q}_M, \boldsymbol{u}_A)$

$I_N = \{i \mid g_{Ni}(t_M, \boldsymbol{q}_M) \leqslant 0\}$

$I_F = \{l \mid l = 2i - 1,\ i \in I_N\} \cup \{l \mid l = 2i,\ i \in I_N\} \cup \{l \mid l = i + 2n_C,\ i \in I_N\}$

$\boldsymbol{W}_{NM} = \{\boldsymbol{w}_N^i(t_M, \boldsymbol{q}_M)\}, \quad \widetilde{\boldsymbol{w}}_{NM} = \{\widetilde{w}_N^i(t_M, \boldsymbol{q}_M)\}, \quad i \in I_N$

$\boldsymbol{W}_{FM} = \{\boldsymbol{w}_F^i(t_M, \boldsymbol{q}_M)\}, \quad \widetilde{\boldsymbol{w}}_{FM} = \{\widetilde{w}_F^i(t_M, \boldsymbol{q}_M)\}, \quad i \in I_F$

$k = 1, \quad \text{converged} = \text{false}, \quad \boldsymbol{\Lambda}_N^k = \boldsymbol{\Lambda}_N(I_N), \quad \boldsymbol{\Lambda}_F^k = \boldsymbol{\Lambda}_F(I_F)$

while converged = false Augmented Lagrangian Method

$\boldsymbol{u}_E = \boldsymbol{u}_A + \boldsymbol{M}_M^{-1}(\boldsymbol{h}_M \Delta t + \boldsymbol{W}_{NM}\boldsymbol{\Lambda}_N^k + \boldsymbol{W}_{FM}\boldsymbol{\Lambda}_F^k)$

$\boldsymbol{q}_E = \boldsymbol{q}_M + \frac{1}{2}\Delta t \boldsymbol{u}_E$

$\boldsymbol{\gamma}_{NE} = \boldsymbol{W}_{NM}^{\mathrm{T}}\boldsymbol{u}_E + \widetilde{\boldsymbol{w}}_{NM}, \quad \boldsymbol{\gamma}_{FE} = \boldsymbol{W}_{FM}^{\mathrm{T}}\boldsymbol{u}_E + \widetilde{\boldsymbol{w}}_{FM}$

$\boldsymbol{\Lambda}_N^{k+1} = \Pi_N(\boldsymbol{\Lambda}_N^k, \boldsymbol{\gamma}_{NE}), \quad \boldsymbol{\Lambda}_F^{k+1} = \Pi_F(\boldsymbol{\Lambda}_N^{k+1}, \boldsymbol{\Lambda}_F^k, \boldsymbol{\gamma}_{FE})$

$\text{error} = \|\boldsymbol{\Lambda}_N^{k+1} - \boldsymbol{\Lambda}_N^k\| + \|\boldsymbol{\Lambda}_F^{k+1} - \boldsymbol{\Lambda}_F^k\|$

converged = (error < tol)

$k = k + 1$

end

$t_E = t_M + \frac{1}{2}\Delta t$ Do the second half time-step

$t^{j+1} = t_E, \quad \boldsymbol{q}^{j+1} = \boldsymbol{q}_E, \quad \boldsymbol{u}^{j+1} = \boldsymbol{u}_E$

$\boldsymbol{\Lambda}_N(I_N) = \boldsymbol{\Lambda}_N^k, \quad \boldsymbol{\Lambda}_F(I_F) = \boldsymbol{\Lambda}_F^k$

end

end

with the Butcher array for the four-stage method ($s = 4$)

$$\begin{array}{c|cccc} 0 & & & & \\ \frac{1}{2} & \frac{1}{2} & & & \\ \frac{1}{2} & 0 & \frac{1}{2} & & \\ 1 & 0 & 0 & 1 & \\ \hline & \frac{1}{6} & \frac{1}{3} & \frac{1}{3} & \frac{1}{6} \end{array} \quad \text{or} \quad \begin{array}{c|c} c & A \\ \hline & b^{\mathrm{T}} \end{array}.$$

The above scheme is a fourth-order integration method for ordinary differential equations, which can be adapted to measure differential equations. For a mechanical system with impacts, one cannot determine accelerations nor contact forces because they are not functions of bounded variation if an impact occurs. Still, for a discretized measure differential equation we are able to define an average acceleration per time-step $\boldsymbol{a}^j = (\boldsymbol{u}^j - \boldsymbol{u}^{j-1})/\Delta t$, which will be denoted by 'pseudo-acceleration'. The average acceleration, taking into account the set-valued behaviour of the contact forces, can be computed with the method of Moreau. A Runge–Kutta method for systems with impact and friction can therefore be formulated, which uses the time-stepping method of Moreau to compute pseudo-accelerations at every stage of the scheme. The Runge–Kutta time-stepping algorithm is summarized in Table 2, which shows how the classical Runge–Kutta method is combined with the time-stepping method of Moreau. The method uses a time-step $\Delta t_2 = \Delta t/4$ for the determination of the pseudo-accelerations. The presented Runge–Kutta time-stepping method is closely related to half-explicit Runge–Kutta methods for differential algebraic equations (Hairer and Wanner, 2002).

Table 2
Runge–Kutta 4 time-stepping method

function $[t, \boldsymbol{q}, \boldsymbol{u}] = \mathit{TimeSteppingMethodRK4}(t_0, t_{\text{end}}, \boldsymbol{q}_0, \boldsymbol{u}_0, N, \text{tol})$
$c = [\,0 \quad \frac{1}{2} \quad \frac{1}{2} \quad 1\,]$
$\Delta t = \frac{t_{\text{end}} - t_0}{N-1}, \quad \Delta t_2 = \Delta t/4$ Initialize
$t^1 = t_0, \quad \boldsymbol{q}^1 = \boldsymbol{q}_0, \quad \boldsymbol{u}^1 = \boldsymbol{u}_0$
$\boldsymbol{\Lambda}_N = \boldsymbol{0}, \quad \boldsymbol{\Lambda}_F = \boldsymbol{0}$
for $j = 1$ **to** N Do all time-steps
$[\boldsymbol{a}_1, \boldsymbol{\Lambda}_N, \boldsymbol{\Lambda}_F] = \mathit{ComputeStage}(t^j, \boldsymbol{q}^j, \boldsymbol{u}^j, \boldsymbol{\Lambda}_N, \boldsymbol{\Lambda}_F, \Delta t_2, \text{tol})$
$\boldsymbol{u}_1 = \boldsymbol{u}^j$
for $m = 2$ **to** 4 Do all stages
$t_m = t^j + c_m \Delta t$
$\boldsymbol{q}_m = \boldsymbol{q}^j + c_m \Delta t \boldsymbol{u}_{m-1}$
$\boldsymbol{u}_m = \boldsymbol{u}^j + c_m \Delta t \boldsymbol{a}_{m-1}$
$[\boldsymbol{a}_m, \boldsymbol{\Lambda}_N, \boldsymbol{\Lambda}_F] = \mathit{ComputeStage}(t_m, \boldsymbol{q}_m, \boldsymbol{u}_m, \boldsymbol{\Lambda}_N, \boldsymbol{\Lambda}_F, \Delta t_2, \text{tol})$
end
$t^{j+1} = t^j + \Delta t$
$\boldsymbol{q}^{j+1} = \boldsymbol{q}^j + (\frac{1}{6}\boldsymbol{u}_1 + \frac{1}{3}\boldsymbol{u}_2 + \frac{1}{3}\boldsymbol{u}_3 + \frac{1}{6}\boldsymbol{u}_4)\Delta t$
$\boldsymbol{u}^{j+1} = \boldsymbol{u}^j + (\frac{1}{6}\boldsymbol{a}_1 + \frac{1}{3}\boldsymbol{a}_2 + \frac{1}{3}\boldsymbol{a}_3 + \frac{1}{6}\boldsymbol{a}_4)\Delta t$
end
end

function $[\boldsymbol{a}_m, \boldsymbol{\Lambda}_N, \boldsymbol{\Lambda}_F] = \mathit{ComputeStage}(t_m, \boldsymbol{q}_m, \boldsymbol{u}_m, \boldsymbol{\Lambda}_N, \boldsymbol{\Lambda}_F, \Delta t_2, \text{tol})$
$t_A = t_m, \quad \boldsymbol{q}_A = \boldsymbol{q}_m, \quad \boldsymbol{u}_A = \boldsymbol{u}_m$
$t_M = t_A + \frac{1}{2}\Delta t_2, \quad \boldsymbol{q}_M = \boldsymbol{q}_A + \frac{1}{2}\Delta t_2 \boldsymbol{u}_A$ Do half a time-step
$\boldsymbol{M}_M = \boldsymbol{M}(t_M, \boldsymbol{q}_M), \quad \boldsymbol{h}_M = \boldsymbol{h}(t_M, \boldsymbol{q}_M, \boldsymbol{u}_A)$
$I_N = \{i \mid g_{Ni}(t_M, \boldsymbol{q}_M) \leqslant 0\}$
$I_F = \{l \mid l = 2i - 1,\ i \in I_N\} \cup \{l \mid l = 2i,\ i \in I_N\} \cup \{l \mid l = i + 2n_C,\ i \in I_N\}$
$\boldsymbol{W}_{NM} = \{\boldsymbol{w}_N^i(t_M, \boldsymbol{q}_M)\}, \quad \widetilde{\boldsymbol{w}}_{NM} = \{\widetilde{w}_N^i(t_M, \boldsymbol{q}_M)\}, \quad i \in I_N$
$\boldsymbol{W}_{FM} = \{\boldsymbol{w}_F^i(t_M, \boldsymbol{q}_M)\}, \quad \widetilde{\boldsymbol{w}}_{FM} = \{\widetilde{w}_F^i(t_M, \boldsymbol{q}_M)\}, \quad i \in I_F$
$k = 1, \quad \text{converged} = \text{false}, \quad \boldsymbol{\Lambda}_N^k = \boldsymbol{\Lambda}_N(I_N), \quad \boldsymbol{\Lambda}_F^k = \boldsymbol{\Lambda}_F(I_F)$
while converged = false Augmented Lagrangian Method
$\boldsymbol{u}_E = \boldsymbol{u}_A + \boldsymbol{M}_M^{-1}(\boldsymbol{h}_M \Delta t_2 + \boldsymbol{W}_{NM}\boldsymbol{\Lambda}_N^k + \boldsymbol{W}_{FM}\boldsymbol{\Lambda}_F^k)$
$\boldsymbol{q}_E = \boldsymbol{q}_M + \frac{1}{2}\Delta t_2 \boldsymbol{u}_E$
$\boldsymbol{\gamma}_{NE} = \boldsymbol{W}_{NM}^{\mathrm{T}}\boldsymbol{u}_E + \widetilde{\boldsymbol{w}}_{NM}, \quad \boldsymbol{\gamma}_{FE} = \boldsymbol{W}_{FM}^{\mathrm{T}}\boldsymbol{u}_E + \widetilde{\boldsymbol{w}}_{FM}$
$\boldsymbol{\Lambda}_N^{k+1} = \Pi_N(\boldsymbol{\Lambda}_N^k, \boldsymbol{\gamma}_{NE}), \quad \boldsymbol{\Lambda}_F^{k+1} = \Pi_F(\boldsymbol{\Lambda}_N^{k+1}, \boldsymbol{\Lambda}_F^k, \boldsymbol{\gamma}_{FE})$
$\text{error} = \|\boldsymbol{\Lambda}_N^{k+1} - \boldsymbol{\Lambda}_N^k\| + \|\boldsymbol{\Lambda}_F^{k+1} - \boldsymbol{\Lambda}_F^k\|$
converged = (error < tol)
$k = k + 1$
end
$\boldsymbol{a}_m = (\boldsymbol{u}_E - \boldsymbol{u}_A)/\Delta t_2$
$\boldsymbol{\Lambda}_N(I_N) = \boldsymbol{\Lambda}_N^k, \quad \boldsymbol{\Lambda}_F(I_F) = \boldsymbol{\Lambda}_F^k$
end

5. The Tippe-Top

In this section we will present a rigid-body model of the Tippe-Top and present numerical results using the Runge–Kutta time-stepping method and Coulomb–Contensou's friction law. The Tippe-Top (Fig. 7) consists of a spherical body with geometric center M, radius r_1, and a stick attached on top of the body. The stick is rounded at the tip with a hemisphere with

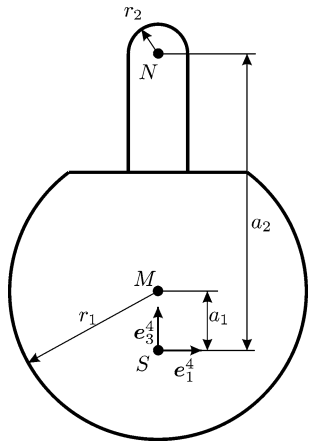

Fig. 7. Geometry of the Tippe-Top.

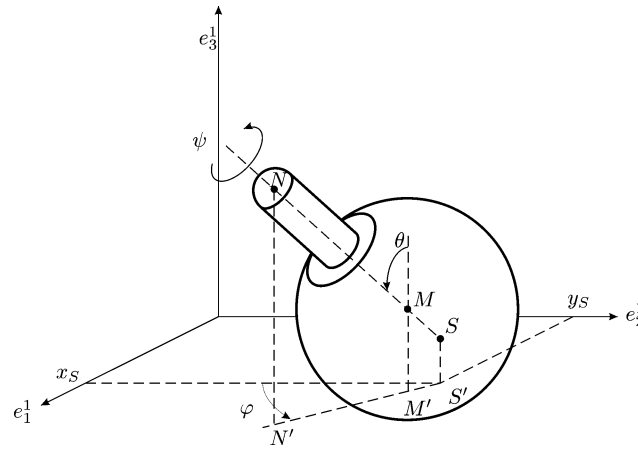

Fig. 8. The Euler angles of the Tippe-Top.

geometric center N and radius r_2. The toy is axisymmetric around the axis MN. The center of mass of the top is S, which lies at a distance a_1 below M and at a distance a_2 from N.

5.1. Coordinate systems

The $\boldsymbol{e}^1 = [\,\boldsymbol{e}_1^1, \boldsymbol{e}_2^1, \boldsymbol{e}_3^1\,]^{\mathrm{T}}$ coordinate frame is the orthonormal absolute coordinate frame fixed to the world where $\boldsymbol{e}_3^1$ points in the vertical direction. The frame $\boldsymbol{e}^4 = [\,\boldsymbol{e}_1^4 \quad \boldsymbol{e}_2^4 \quad \boldsymbol{e}_3^4\,]^{\mathrm{T}}$ is fixed to the body with $\boldsymbol{e}_3^4$ along the axis of symmetry. The frame $\boldsymbol{e}^4$ results from the frame $\boldsymbol{e}^1$ after a sequence of three elementary rotations $\boldsymbol{e}^2 = \boldsymbol{A}^{21}\boldsymbol{e}^1$, $\boldsymbol{e}^3 = \boldsymbol{A}^{32}\boldsymbol{e}^2$, $\boldsymbol{e}^4 = \boldsymbol{A}^{43}\boldsymbol{e}^3$, where $\boldsymbol{e}^2$ and $\boldsymbol{e}^3$ are intermediate frames. The total directional cosine matrix is composed by multiplication of the cosine matrices of the elementary rotations $\boldsymbol{e}^4 = \boldsymbol{A}^{41}\boldsymbol{e}^1$ with $\boldsymbol{A}^{41} = \boldsymbol{A}^{43}\boldsymbol{A}^{32}\boldsymbol{A}^{21}$. We will describe the rotation of the top in Euler angles.

The Euler angles are θ (nutation), φ (precession) and ψ (spin angle), see Fig. 8. The sequence of rotations consists of a rotation φ around $\boldsymbol{e}_3^1$, then a rotation θ around $\boldsymbol{e}_1^2$ and finally a rotation ψ around $\boldsymbol{e}_3^3$. The resulting total directional cosine matrix for Euler angles becomes $\boldsymbol{A}^{41} = \boldsymbol{A}^{43}(\psi)\boldsymbol{A}^{32}(\theta)\boldsymbol{A}^{21}(\varphi)$ with

$$\boldsymbol{A}^{43}(\psi) = \begin{bmatrix} \cos\psi & \sin\psi & 0 \\ -\sin\psi & \cos\psi & 0 \\ 0 & 0 & 1 \end{bmatrix}, \quad \boldsymbol{A}^{32}(\theta) = \begin{bmatrix} 1 & 0 & 0 \\ 0 & \cos\theta & \sin\theta \\ 0 & -\sin\theta & \cos\theta \end{bmatrix}, \quad \boldsymbol{A}^{21}(\varphi) = \begin{bmatrix} \cos\varphi & \sin\varphi & 0 \\ -\sin\varphi & \cos\varphi & 0 \\ 0 & 0 & 1 \end{bmatrix}. \tag{5.1}$$

The vector of Poisson of the top can expressed in the Euler angles

$$\begin{aligned} \boldsymbol{\omega} &= \dot{\varphi}\boldsymbol{e}_3^1 + \dot{\theta}\boldsymbol{e}_1^2 + \dot{\psi}\boldsymbol{e}_3^3 = \boldsymbol{e}^{1\mathrm{T}}\begin{bmatrix} 0 \\ 0 \\ \dot{\varphi} \end{bmatrix} + \boldsymbol{e}^{2\mathrm{T}}\begin{bmatrix} \dot{\theta} \\ 0 \\ 0 \end{bmatrix} + \boldsymbol{e}^{3\mathrm{T}}\begin{bmatrix} 0 \\ 0 \\ \dot{\psi} \end{bmatrix} \\ &= \boldsymbol{e}^{1\mathrm{T}}\begin{bmatrix} 0 \\ 0 \\ \dot{\varphi} \end{bmatrix} + \boldsymbol{e}^{1\mathrm{T}}\boldsymbol{A}^{12}\begin{bmatrix} \dot{\theta} \\ 0 \\ 0 \end{bmatrix} + \boldsymbol{e}^{1\mathrm{T}}\boldsymbol{A}^{13}\begin{bmatrix} 0 \\ 0 \\ \dot{\psi} \end{bmatrix} = \omega_1^1\boldsymbol{e}_1^1 + \omega_2^1\boldsymbol{e}_2^1 + \omega_3^1\boldsymbol{e}_3^1 \\ &= \boldsymbol{e}^{4\mathrm{T}}\boldsymbol{A}^{41}\begin{bmatrix} 0 \\ 0 \\ \dot{\varphi} \end{bmatrix} + \boldsymbol{e}^{4\mathrm{T}}\boldsymbol{A}^{42}\begin{bmatrix} \dot{\theta} \\ 0 \\ 0 \end{bmatrix} + \boldsymbol{e}^{4\mathrm{T}}\boldsymbol{A}^{43}\begin{bmatrix} 0 \\ 0 \\ \dot{\psi} \end{bmatrix} = \omega_1^4\boldsymbol{e}_1^4 + \omega_2^4\boldsymbol{e}_2^4 + \omega_3^4\boldsymbol{e}_3^4, \end{aligned} \tag{5.2}$$

with

$$\begin{bmatrix} \omega_1^1 \\ \omega_2^1 \\ \omega_3^1 \end{bmatrix} = \begin{bmatrix} \dot{\theta}\cos\varphi + \dot{\psi}\sin\varphi\sin\theta \\ \dot{\theta}\sin\varphi - \dot{\psi}\cos\varphi\sin\theta \\ \dot{\varphi} + \dot{\psi}\cos\theta \end{bmatrix}, \qquad \begin{bmatrix} \omega_1^4 \\ \omega_2^4 \\ \omega_3^4 \end{bmatrix} = \begin{bmatrix} \dot{\varphi}\sin\theta\sin\psi + \dot{\theta}\cos\psi \\ \dot{\varphi}\sin\theta\cos\psi - \dot{\theta}\sin\psi \\ \dot{\psi} + \dot{\varphi}\cos\theta \end{bmatrix}. \tag{5.3}$$

5.2. Equations of motion in Euler angles

As generalized coordinates for the top we choose the positions x_S, y_S and z_S along the axes $\boldsymbol{e}_1^1$, $\boldsymbol{e}_2^1$, $\boldsymbol{e}_3^1$ to describe the translational motion of the center of mass S and the Euler angles θ, φ and ψ to describe the rotational motion:

$$\boldsymbol{q} = [\,x_S \quad y_S \quad z_S \quad \theta \quad \varphi \quad \psi\,]^{\mathrm{T}}. \tag{5.4}$$

The kinetic energy T can be expressed in the generalized coordinates

$$\begin{aligned} T &= \frac{1}{2}m\left(\dot{x}_S^2+\dot{y}_S^2+\dot{z}_S^2\right)+\frac{1}{2}I_1\left(\omega_1^4\right)^2+\frac{1}{2}I_2\left(\omega_2^4\right)^2+\frac{1}{2}I_3\left(\omega_3^4\right)^2 \\ &= \frac{1}{2}m\left(\dot{x}_S^2+\dot{y}_S^2+\dot{z}_S^2\right)+\frac{1}{2}I_1\left(\dot{\varphi}^2\sin^2\theta+\dot{\theta}^2\right)+\frac{1}{2}I_3\left(\dot{\psi}+\dot{\varphi}\cos\theta\right)^2, \end{aligned} \tag{5.5}$$

with $I_1 = I_2$ due to axisymmetry. The potential energy V is purely due to gravity

$$V = mgz_S. \tag{5.6}$$

The Lagrange's equation of motion for the unconstrained undamped motion is

$$\frac{\mathrm{d}}{\mathrm{d}t}T_{,\dot{q}} - T_{,q} + V_{,q} = 0, \tag{5.7}$$

which yields

$$\begin{aligned} &m\ddot{x}_S = 0, \quad m\ddot{y}_S = 0, \quad m\ddot{z}_S + mg = 0, \\ &I_1\ddot{\theta} - (I_1 - I_3)\dot{\varphi}^2\sin\theta\cos\theta + I_3\dot{\psi}\dot{\varphi}\sin\theta = 0, \\ &\left(I_1\sin^2\theta + I_3\cos^2\theta\right)\ddot{\varphi} + I_3\ddot{\psi}\cos\theta + 2(I_1 - I_3)\dot{\varphi}\dot{\theta}\sin\theta\cos\theta - I_3\dot{\psi}\dot{\theta}\sin\theta = 0, \\ &I_3(\ddot{\psi} + \ddot{\varphi}\cos\theta - \dot{\varphi}\dot{\theta}\sin\theta) = 0. \end{aligned} \tag{5.8}$$

The equations of motion can be put in the form $\boldsymbol{M}(\boldsymbol{q})\ddot{\boldsymbol{q}} - \boldsymbol{h}(\boldsymbol{q},\dot{\boldsymbol{q}}) = \boldsymbol{0}$, where $\boldsymbol{M}$ is the mass matrix and $\boldsymbol{h}$ is a vector containing gyroscopical and gravitational forces with

$$\boldsymbol{M} = \begin{bmatrix} m & 0 & 0 & 0 & 0 & 0 \\ 0 & m & 0 & 0 & 0 & 0 \\ 0 & 0 & m & 0 & 0 & 0 \\ 0 & 0 & 0 & I_1 & 0 & 0 \\ 0 & 0 & 0 & 0 & I_1\sin^2\theta + I_3\cos^2\theta & I_3\cos\theta \\ 0 & 0 & 0 & 0 & I_3\cos\theta & I_3 \end{bmatrix}, \qquad \boldsymbol{h} = \begin{bmatrix} 0 \\ 0 \\ -mg \\ \left((I_1 - I_3)\dot{\varphi}\cos\theta - I_3\dot{\psi}\right)\dot{\varphi}\sin\theta \\ \left(2(I_3 - I_1)\dot{\varphi}\cos\theta + I_3\dot{\psi}\right)\dot{\theta}\sin\theta \\ I_3\dot{\varphi}\dot{\theta}\sin\theta \end{bmatrix}. \tag{5.9}$$

5.3. Constraints

The top has two contact points (either open or closed). Contact point 1 is the contact between the body and the floor. Contact point 2 is the contact between the hemispherical tip of the stick and the floor. The point on the spherical part of the top, being closest to the projection point M', is called point C. Contact is established when C agrees with M' and then we call C the contact point. The location of C is given by

$$\boldsymbol{r}_C = \boldsymbol{r}_S + \boldsymbol{r}_{SM} + \boldsymbol{r}_{MC}, \tag{5.10}$$

with

$$\boldsymbol{r}_S = \boldsymbol{e}^{1\mathrm{T}}\begin{bmatrix} x_S \\ y_S \\ z_S \end{bmatrix}, \qquad \boldsymbol{r}_{SM} = \boldsymbol{e}^{4\mathrm{T}}\begin{bmatrix} 0 \\ 0 \\ a_1 \end{bmatrix} = \boldsymbol{e}^{1\mathrm{T}}\boldsymbol{A}^{14}\begin{bmatrix} 0 \\ 0 \\ a_1 \end{bmatrix}, \qquad \boldsymbol{r}_{MC} = \boldsymbol{e}^{1\mathrm{T}}\begin{bmatrix} 0 \\ 0 \\ -r_1 \end{bmatrix}. \tag{5.11}$$

The vector $\boldsymbol{r}_C$ expressed in Euler angles becomes

$$\boldsymbol{r}_C = \begin{bmatrix} x_S + a_1\sin\varphi\sin\theta \\ y_S - a_1\cos\varphi\sin\theta \\ z_S + a_1\cos\theta - r_1 \end{bmatrix}, \tag{5.12}$$

from which the normal contact distance of contact 1 can be obtained

$$g_{N1} = \boldsymbol{r}_{C3} = z_S + a_1\cos\theta - r_1. \tag{5.13}$$

Similarly, the contact distance between the stick and the floor reads as

$$g_{N2} = z_S + a_2\cos\theta - r_2. \tag{5.14}$$

The contact distances have the derivatives $\gamma_{Ni} = \dot{g}_{Ni}$ (almost everywhere)

$$\gamma_{Ni} = \dot{z}_S - a_i\dot{\theta}\sin\theta, \quad i = 1,2, \tag{5.15}$$

or $\gamma_{Ni} = \boldsymbol{W}_{Ni}^{\mathrm{T}}\dot{\boldsymbol{q}} + \widetilde{w}_{Ni}$ with

$$\boldsymbol{W}_{Ni} = [\,0 \quad 0 \quad 1 \quad -a_i \sin\theta \quad 0 \quad 0\,]^{\mathrm{T}}, \qquad \widetilde{w}_{Ni} = 0. \tag{5.16}$$

The velocity of point C on the spherical part top is given by

$$\boldsymbol{v}_C = \boldsymbol{v}_S + \boldsymbol{\omega} \times \boldsymbol{r}_{SC}, \tag{5.17}$$

where $\boldsymbol{r}_{SC}$ is the vector from the center of mass S to the point C, i.e., $\boldsymbol{r}_{SC} = \boldsymbol{r}_C - \boldsymbol{r}_S$. The velocity $\boldsymbol{v}_C$ in the frame $\boldsymbol{e}^1$ becomes

$$\boldsymbol{v}_C^1 = \begin{bmatrix} \dot{x}_S + (a_1\dot{\varphi} + r_1\dot{\psi})\sin\theta\cos\varphi + \dot{\theta}(a_1\cos\theta - r_1)\sin\varphi \\ \dot{y}_S + (a_1\dot{\varphi} + r_1\dot{\psi})\sin\theta\sin\varphi - \dot{\theta}(a_1\cos\theta - r_1)\cos\varphi \\ \dot{z}_S - a_1\dot{\theta}\sin\theta \end{bmatrix}, \tag{5.18}$$

where the component in $\boldsymbol{e}_3^1$ is zero when $\gamma_{N1} = 0$.

The tangential contact velocity is a vector in the $(\boldsymbol{e}_1^1, \boldsymbol{e}_2^1)$ plane. The tangential contact velocity at contact point 1 is given by the components of $\boldsymbol{v}_C^1$ in the $(\boldsymbol{e}_1^1, \boldsymbol{e}_2^1)$ directions

$$\boldsymbol{\gamma}_{T1} = \begin{bmatrix} \dot{x}_S + (a_1\dot{\varphi} + r_1\dot{\psi})\sin\theta\cos\varphi + \dot{\theta}(a_1\cos\theta - r_1)\sin\varphi \\ \dot{y}_S + (a_1\dot{\varphi} + r_1\dot{\psi})\sin\theta\sin\varphi - \dot{\theta}(a_1\cos\theta - r_1)\cos\varphi \end{bmatrix}. \tag{5.19}$$

In the same way we can find $\boldsymbol{\gamma}_{T2}$, which we write in the form $\boldsymbol{\gamma}_{Ti} = \boldsymbol{W}_{Ti}^{\mathrm{T}}\dot{\boldsymbol{q}} + \widetilde{\boldsymbol{w}}_{Ti}$ with $i = 1, 2$ and

$$\boldsymbol{W}_{Ti} = \begin{bmatrix} 1 & 0 & 0 & (a_i\cos\theta - r_i)\sin\varphi & a_i\sin\theta\cos\varphi & r_i\sin\theta\cos\varphi \\ 0 & 1 & 0 & -(a_i\cos\theta - r_i)\cos\varphi & a_i\sin\theta\sin\varphi & r_i\sin\theta\sin\varphi \end{bmatrix}^{\mathrm{T}}, \qquad \widetilde{\boldsymbol{w}}_{Ti} = \begin{bmatrix} 0 \\ 0 \end{bmatrix}. \tag{5.20}$$

The relative spin of a contact point is the projection of the Poisson vector on the $\boldsymbol{e}_3^1$ axis, i.e., ω_3^1. The spin velocity vector is the product of spin angular velocity and a contact radius R_i and given by $\gamma_{\tau i} = \omega_3^1 R_i = (\dot{\phi} + \dot{\psi}\cos\theta)R_i$. The contact matrices can be found in a straightforward way:

$$\boldsymbol{W}_{\tau i} = [\,0 \quad 0 \quad 0 \quad 0 \quad 1 \quad \cos\theta\,]^{\mathrm{T}} R_i, \qquad \widetilde{w}_{\tau i} = 0. \tag{5.21}$$

5.4. Numerical results

Some numerical results on the Tippe-Top with Coulomb–Contensou friction will be presented in this subsection. We will show that Coulomb–Contensou friction is important for the dynamics of the top. The stability and dynamics of the Tippe-Top will only be briefly discussed. We refer to Magnus (1971) for a more complete analysis of the stability of the equilibrium positions.

Numerical results on the Tippe-Top with an approximated Coulomb–Contensou friction model (tangens hyperbolicus approximation) and a penalty approximation in the normal direction were given in Friedl (1997). We will present similar results, but making use of the set-valued Coulomb–Contensou friction law in tangential direction and Signorini's law in normal direction. We consider for the numerical analysis the same dataset as taken in Friedl (1997):

Dynamics: $m = 6 \times 10^{-3}$ kg , $I_1 = 8 \times 10^{-7}$ kg $\cdot$ m^2, $I_3 = 7 \times 10^{-7}$ kg $\cdot$ m^2, $g = 9.81$ m/s^2;

Geometry: $a_1 = 0.3 \times 10^{-2}$ m, $a_2 = 1.6 \times 10^{-2}$ m, $r_1 = 1.5 \times 10^{-2}$ m, $r_2 = 0.5 \times 10^{-2}$ m;

Contact: $\mu_i = 0.3$, $\varepsilon_{Ni} = 0$, $R_i = 5 \times 10^{-4}$ m for $i = 1, 2$.

The parameters of the above dataset are realistic for a wooden commercial Tippe-Top. The contact parameters depend on the Tippe-Top as well as on the supporting underground. A friction coefficient $\mu = 0.3$ is realistic for dry contact of wood on wood. Hardly any restitution is observed when a wooden Tippe-Top is dropped on a wooden table or floor, which is well modelled with a completely inelastic impact condition $\varepsilon_N = 0$. A more difficult parameter to choose is the contact radius R. The radius of the contact surface would be according to Hertz law (3.2)

$$R_{\mathrm{Hertz}} = \left(\frac{3\varrho^*\lambda_N}{4E^*}\right)^{1/3}.$$

We assume that the underground is flat and therefore that $\varrho^* = r_1$. The contact force is approximately equal to its stationary value $\lambda_N \approx mg$. Furthermore, we assume the effective modulus of elasticity to be $E^* = 5$ GPa, which is realistic for a wooden toy on a wooden surface. The theoretical radius R_{Hertz} would with these assumptions be about 5×10^{-5} m, which is much less than the surface roughness of wood (10^{-4}–10^{-3} m). It can therefore be expected that the radius of the contact surface does not follow Hertz' law but depends on the roughness of the contacting bodies. We therefore assume a constant contact radius of $R = 5 \times 10^{-4}$ m for both contact points. The influence of the contact radius on the dynamics of the system will be studied at the end of this section.

Using the above dataset, the motion of the Tippe-Top was simulated with the four stage Runge–Kutta time-stepping method and with the initial condition (following Friedl, 1997)

$$z_{S0} = 1.2015 \times 10^{-2} \text{ m}, \qquad \theta_0 = 0.1 \text{ rad}, \qquad \dot{\psi}_0 = 180 \text{ rad/s},$$

and all other initial states being equal to zero. The time-history of the inclination θ during the first 8 seconds of the motion is shown in Fig. 9 and the contact distances in Fig. 10. The initial condition at $t = 0$ s corresponds to a slightly inclined top which is resting with its body on the floor, i.e., $g_{N1} = 0$ and $g_{N2} > 0$, and is spinning fastly around its axis of revolution. The friction forces in the contact surface cause a frictional torque along the $\boldsymbol{e}_3^1$ axis. The frictional torque together with the spin around the $\boldsymbol{e}_3^4$ axis causes a gyroscopical torque around the nodal axis $\boldsymbol{e}_1^2$ which slowly inverts the orientation of the top, $\theta = 0 \to \theta = \pi$. A high-frequency nutational oscillation is superimposed on the global motion of the top. The stick touches the floor at $t = 1.5$ s, after which the body loses contact with the floor, i.e., $g_{N1} > 0$ and $g_{N2} = 0$. The top turns almost completely upright on the stick during the period $1.6 < t < 4$ s. The rotational speed of the top is gradually reduced due to the dissipation of the friction forces, which causes a re-inversion of the top, $t > 4$ s. The re-inversion causes the body to touch the floor at $t = 4.55$ s. A rocking motion is initiated, which ends in an accumulation point of impacts. The top remains in double-point contact ($g_{N1} = g_{N2} = 0$) during the period $4.65 < t < 5.4$ s. Finally, the contact between stick and floor is opened and the top gradually turns to its trivial non-rotating equilibrium position.

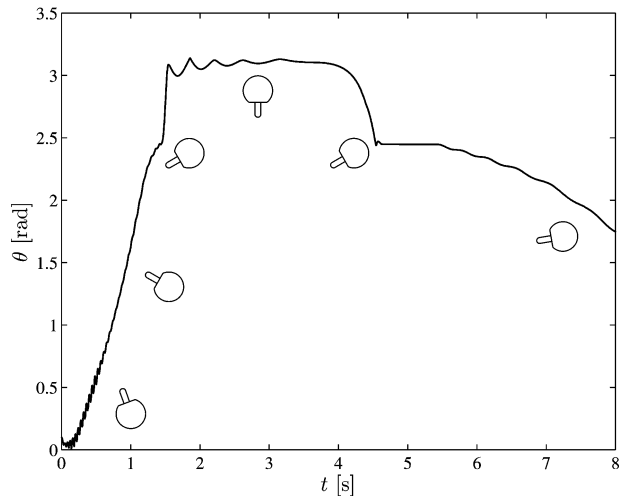

Fig. 9. Time-history of the inclination of the Tippe-Top ($R = 5 \times 10^{-4}$ m).

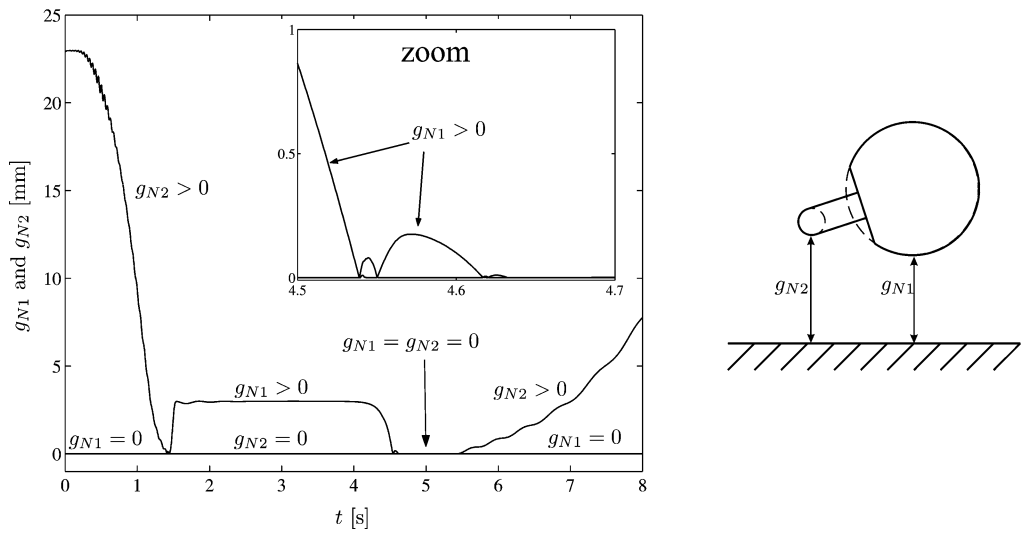

Fig. 10. Time-history of the contact distances of the Tippe-Top ($R = 5 \times 10^{-4}$ m).

5.5. Local stability analysis of equilibria

Stationary motion of the Tippe-Top can occur in the trivial position ($\theta = 0$) with contact between the body and the floor or in an inverted position ($\theta = \pi$) with contact between the stick and the floor. The stability of these equilibria depends on the spin ω and on the geometry of the top. Dissipation will slow down the top and bring it back to rest. Still, it is of interest to know whether the top can stay (for some time) on its stick for a certain spin ω and whether the trivial position can become (temporarily) unstable for large values of ω. We will therefore study the local (quasi)-stability of the Tippe-Top under the assumption that the spin ω is constant, i.e., $\omega = \omega_0$. The description of the top in Euler angles becomes singular for the equilibrium positions ($\theta = 0, \pi$). In the sequel we will make use of the equations of motion of the Tippe-Top in Cardan angles α, β, γ for small angles around the equilibria. The derivation of the equations in Cardan angles will be omitted here for brevity but can be found in Magnus (1971).

The two equilibria show a similarity and it will therefore prove to be convenient to introduce the following parameters

(1) body-floor contact: $a = a_1 > 0$, $r = r_1 > 0$, $r > a$,
(2) stick-floor contact: $a = -a_2 < 0$, $r = r_2 > 0$, $r > a$.

For each case the value of $h = -a + r$, which defines the maximal height of the center of mass S with respect to the floor, is positive $h > 0$. Stationary motion is defined by $\alpha = \beta = 0$, $\dot\gamma = \omega_0$. The quantities α, β, $\dot\alpha$, $\dot\beta$ and $\dot x_S, \dot y_S$ are small of first order $\mathrm{O}(\eta)$. The equations of motion in Cardan angles for small angles become (Magnus, 1971)

$$\begin{aligned}
&m\ddot x_S = \lambda_{T1},\\
&m\ddot y_S = \lambda_{T2},\\
&m\ddot z_S = -mg + \lambda_N,\\
&I_1\ddot\alpha + I_3\dot\gamma\dot\beta = -a\alpha\lambda_N + h\lambda_{T2} + \mathrm{O}\big(\eta^3\big),\\
&I_1\ddot\beta - I_3\dot\gamma\dot\alpha = -a\beta\lambda_N - h\lambda_{T1} + \mathrm{O}\big(\eta^3\big),\\
&I_3\dot\gamma = r\alpha\lambda_{T1} + r\beta\lambda_{T2} + \mathrm{O}\big(\eta^2\big).
\end{aligned} \tag{5.22}$$

The term $m\ddot z_S$ is of order $\mathrm{O}(\eta)$, which is small with respect to the term $-mg$. It follows that $\lambda_N = mg$. If λ_{T1} and λ_{T2} are of first order $\mathrm{O}(\eta)$ then it follows that $I_3\dot\gamma$ is of order $\mathrm{O}(\eta^2)$, which we neglect, and which agrees with the assumption $\dot\gamma = \omega_0 = \text{constant}$.

Magnus (1971) presented the necessary and sufficient conditions for local stability of the Tippe-Top in the presence of a smooth friction law. The proof is based on a linear stability analysis by means of eigenvalues. In this subsection we will give a similar local stability analysis based on the Coulomb–Contensou friction law, which gives a smooth friction characteristic $\boldsymbol\lambda_T(\boldsymbol\gamma_T)$ for nonzero spin ω.

The tangential friction force is for $u = v/(\omega R) < 1$ given by (3.17)

$$-\boldsymbol\lambda_T \in \partial_{\boldsymbol\gamma_T}\|\boldsymbol\gamma_T\|\frac{3\mu\lambda_N}{32}\pi u\big(-u^2+4\big), \quad u \leqslant 1, \tag{5.23}$$

from which we can derive for small u the smooth relation

$$\boldsymbol\lambda_T \approx -\mu\lambda_N\frac{3}{8\pi}\frac{1}{\omega R}\boldsymbol\gamma_T = -\varepsilon\boldsymbol\gamma_T, \tag{5.24}$$

with

$$\varepsilon = \mu mg\frac{3}{8\pi}\frac{1}{\omega R}. \tag{5.25}$$

Note that $\boldsymbol\lambda_T$ is of order $\mathrm{O}(\eta)$ and that $\lambda_N \approx mg$. The reduced equations of motion become

$$\begin{aligned}
&m\dot v_x = -\varepsilon(v_x - h\dot\beta + r\omega_0\alpha),\\
&m\dot v_y = -\varepsilon(v_y + h\dot\alpha + r\omega_0\beta),\\
&I_1\ddot\alpha + \varepsilon h^2\dot\alpha + amg\alpha + I_3\omega_0\dot\beta + \varepsilon rh\omega_0\beta + \varepsilon hv_y = 0,\\
&I_1\ddot\beta + \varepsilon h^2\dot\beta + amg\beta - I_3\omega_0\dot\alpha - \varepsilon rh\omega_0\alpha - \varepsilon hv_x = 0,
\end{aligned} \tag{5.26}$$

with $v_x = \dot x_S$ and $v_y = \dot y_S$. Using the complex variables

$$w = v_x + \mathrm{i}v_y, \qquad \xi = \alpha + \mathrm{i}\beta, \tag{5.27}$$

the reduced equations of motion (5.26) can be transformed into the complex system of differential equations

$$\begin{aligned} &m\dot{w} + \varepsilon(w + \mathrm{i}h\dot{\xi} + r\omega_0\xi) = 0,\\ &I_1\ddot{\xi} + \varepsilon h^2\dot{\xi} + amg\xi - \mathrm{i}I_3\omega_0\dot{\xi} - \mathrm{i}\varepsilon rh\omega_0\xi - \mathrm{i}\varepsilon hw = 0. \end{aligned} \tag{5.28}$$

With the ansatz

$$w = W\,\mathrm{e}^{\lambda t}, \qquad \xi = \Xi\,\mathrm{e}^{\lambda t}, \tag{5.29}$$

we obtain the characteristic equation

$$\det\begin{bmatrix} m\lambda + \varepsilon & \mathrm{i}\varepsilon h\lambda + \varepsilon r\omega_0 \\ -\mathrm{i}\varepsilon h & I_1\lambda^2 + (\varepsilon h^2 - \mathrm{i}I_3\omega_0)\lambda + amg - \mathrm{i}\varepsilon rh\omega_0 \end{bmatrix} = 0 \tag{5.30}$$

or

$$m\lambda\big[I_1\lambda^2 - \mathrm{i}I_3\omega_0\lambda + amg\big] + \varepsilon\big[\big(I_1 + mh^2\big)\lambda^2 - \mathrm{i}(I_3 + mhr)\omega_0\lambda + amg\big] = 0. \tag{5.31}$$

Following Magnus (1971), the system will be on the verge of instability when λ is purely imaginary. Both expressions between the straight brackets will be real valued if λ is purely imaginary. The first expression between straight brackets is, however, multiplied by λ. It therefore must hold that both expressions between the straight brackets must vanish and we obtain

$$mh\lambda(h\lambda - \mathrm{i}r\omega_0) = 0, \tag{5.32}$$

which has two roots. The first root $\lambda = 0$ of (5.32) is not a root of the characteristic equation (5.31). Substitution of the second root of (5.32), $\lambda = \mathrm{i}r\omega_0/h$, in one of the bracket expressions of (5.31) gives the condition

$$I_1\frac{r}{h}\left(\frac{I_3}{I_1} - \frac{r}{h}\right)\omega_0^2 + amg = 0, \tag{5.33}$$

which defines the (local) stability boundary. In the locally stable region it must hold that

$$I_1\frac{r}{h}\left(\frac{I_3}{I_1} - \frac{r}{h}\right)\omega_0^2 > -amg. \tag{5.34}$$

Consequently, the trivial position of the non-rotating Tippe-Top is stable if $a > 0$, as expected ($a > 0$ means that the center of mass is located below the center of rotation). Following Magnus (1971), we study the stability of the Tippe-Top in the $(h/r, I_3/I_1)$ plane (Fig. 11). We will only consider the strip $0 < I_3/I_1 < 2$. This strip is divided in four regions by

the line $\quad \dfrac{h}{r} = 1,$

on which $a = 0$, and

the hyperbole $\quad \dfrac{h}{r} = \dfrac{I_1}{I_3}.$

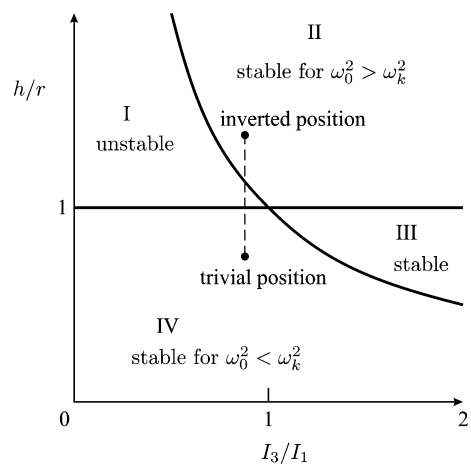

Fig. 11. Stability diagram of the Tippe-Top (Magnus, 1971).

- *Region* I: $1 < h/r < I_1/I_3$. Because $h = -a + r > r$ it must hold that $a < 0$. The left-hand side of (5.34) is negative while the right-hand side is positive. The stationary point is therefore unstable for all values of ω_0.
- *Region* II: $1 < h/r;\ I_1/I_3 < h/r$. The right-hand side of (5.34) is positive because $a < 0$. The stationary point is locally asymptotically stable if $\omega_0^2 > \omega_k^2$ with

$$\omega_k^2 = -\frac{amg}{(r/h)I_1(I_3/I_1 - r/h)} > 0. \tag{5.35}$$

  The stationary point is unstable if $\omega_0^2 < \omega_k^2$.
- *Region* III: $1 > h/r > I_1/I_3$. The right-hand side of (5.34) is negative because $a > 0$. The left-hand side of (5.34) is non-negative for all values of ω_0. The stationary point is always locally asymptotically stable (for $\omega_0 \neq 0$).
- *Region* IV: $1 > h/r;\ I_1/I_3 > h/r$. The right-hand side of (5.34) is negative because $a > 0$. The stationary point is locally asymptotically stable if $0 < \omega_0^2 < \omega_k^2$ and unstable if $\omega_0^2 > \omega_k^2$. The stability regions together with the trivial and inverted position of the Tippe-Top are depicted in Fig. 11.

A commercial Tippe-Top is designed such that the trivial position is located in region IV, which can become unstable, and the inverted position is located in region II and can be stable for large values of ω_0. The stability regions do not depend on ε and do therefore not depend on the contact radius $R > 0$, but the magnitude of the eigenvalues does depend on ε and R. However, if the contact radius tends to zero $R \downarrow 0$, then the value of ε becomes very large. Dividing the characteristic equation (5.31) by ε and neglecting terms $1/\varepsilon$ gives the characteristic equation

$$\left(I_1 + mh^2\right)\lambda^2 - \mathrm{i}(I_3 + mhr)\omega_0\lambda + amg = 0, \tag{5.36}$$

which has the eigenvalues

$$\lambda = \mathrm{i}\left(\frac{B}{2A} \pm \sqrt{\frac{B^2}{4A^2} + \frac{C}{A}}\right), \quad \text{with } A = I_1 + mh^2,\ B = (I_3 + mhr)\omega_0,\ C = amg. \tag{5.37}$$

The eigenvalues (5.37) are for the trivial equilibrium ($a > 0$ and therefore $C > 0$) always purely imaginary (non-hyperbolic case). The real part of the eigenvalues will therefore be very small for small values of the contact radius R.

Fig. 12 shows numerical simulations of the Tippe-Top for three values of the contact radius. Apparently, a smaller contact radius causes a slower inversion of the Tippe-Top. This can be explained by the fact that decreasing the contact radius also decreases the magnitude of the real part of the eigenvalues. This shows the importance of Coulomb–Contensou's friction law for the dynamics of the system.

Consider the case that only Coulomb friction is assumed, implying a zero contact radius. Furthermore, assume that the Tippe-Top is initiated close to its trivial equilibrium and with a pure-rolling initial condition ($\theta \ll 1$ and $\boldsymbol{\gamma}_T = \mathbf{0}$). If the friction coefficient μ is sufficiently large, then the Tippe-Top will perform a pendulum motion around the trivial equilibrium, purely rolling over the floor, with a frequency given by (5.37). Additional dissipation due to air resistance will even damp out the oscillation. The friction coefficient must be sufficiently large to prevent stick-slip transitions during the pure rolling oscillation.

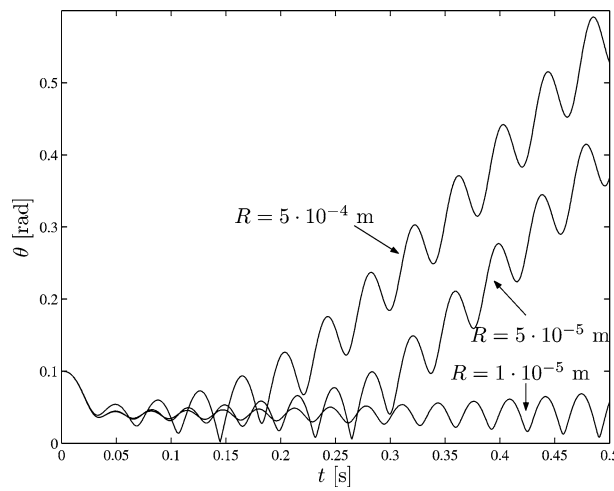

Fig. 12. Time-history of the inclination for different contact radii.

The question arises whether the trivial equilibrium is locally stable under the assumption of Coulomb friction. A consideration taking only the sticking (i.e., pure rolling) motion into account would indeed point in the direction of stability. However, if the spin ω is large enough, then there might exist slipping initial conditions arbitrary close to the trivial equilibrium for which the motion diverges from the equilibrium leading to an inversion of the Tippe-Top. It can therefore not be concluded that the trivial equilibrium is locally stable in the sense of Lyapunov. Still, the Tippe-Top would under the assumption of Coulomb friction not invert at all if it was initiated with a pure rolling initial condition. Observations on the Tippe-Top, which show inversion of a fastly spinning top for arbitrary initial conditions, indicate that Coulomb–Contensou friction is indeed relevant.

6. Conclusion

A set-valued force law to describe spatial Coulomb–Contensou friction was presented in this paper. The set-valued friction law was formulated within the theory of non-smooth potentials and is able to describe the smooth nature of the friction forces during slipping/spin as well as the set-valued nature of the friction forces during stick (no slipping, no spin). The friction model, presented here, augments the existing set-valued law for spatial Coulomb friction by taking drilling friction and spin into account (according to the law of Contensou). Other contact and friction effects, such as adhesion and rolling friction, might be described within the same framework.

A higher-order Runge–Kutta time-stepping method was presented in this paper as an extension to the existing time-stepping method of Moreau. The need for such a higher-order integration method became apparent during the numerical analysis of the Tippe-Top. The Tippe-Top experiences almost no damping and exhibits high-frequency oscillation in the nutation. Numerical simulation with the classical (low-order) time-stepping method yielded fastly diverging solutions, or a fast deadening of the nutational oscillation if integrated with a fully implicit version of the classical time-stepping method. Reducing the step-size led to different results as the divergence or deadening was weakened. The presented higher-order Runge–Kutta method gives the correct result and converges for a reduction of the step-size. Further research will focus on establishing a fundamental background for higher-order time-stepping methods within the framework of DAE-solvers and on the development of automatic variable step-size schemes.

The algebraic inclusion, formed by the equation of motion and the set-valued contact laws, was numerically solved in this paper by making use of the Augmented Lagrangian Method. The LCP or NCP formulation of the contact problem, formerly used by the authors, was abandoned as it became fully impractical when applied to Coulomb–Contensou friction. A substantial advantage of the Augmented Lagrangian approach is, that it solves the algebraic inclusion for arbitrary admissible sets of contact forces (e.g., the set B_F). Other contact laws, which might be even more exotic due to for instance anisotropy, can therefore still be handled with the Augmented Lagrangian approach.

The importance of Coulomb–Contensou friction for the dynamics of mechanical systems was illustrated in this paper by an analysis on the Tippe-Top. Industrial applications with fairly rigid contact between spinning objects, such as ball bearings, grinding devices and drillstrings for oil-wells, motivate research on Coulomb–Contensou friction within a non-smooth formalism.

Appendix A. Integral tables

Use has been made of the following integrals which can be found in Bronstein and Semendjajew (1984). The integrals contain the expression $X = ax^2 + bx + c$ with $a < 0$ and $\Delta = 4ac - b^2 < 0$.

$$\int x^2\sqrt{X}\,\mathrm{d}x = \left(x - \frac{5b}{6a}\right)\frac{X\sqrt{X}}{4a} + \frac{5b^2 - 4ac}{16a^2}\int \sqrt{X}\,\mathrm{d}x, \tag{A.1}$$

$$\int \sqrt{X}\,\mathrm{d}x = \frac{2ax + b}{4a}\sqrt{X} + \frac{\Delta}{8a}\int \frac{\mathrm{d}x}{\sqrt{X}}, \tag{A.2}$$

$$\int \frac{\mathrm{d}x}{\sqrt{X}} = -\frac{1}{\sqrt{-a}}\arcsin\frac{2ax + b}{\sqrt{-\Delta}}, \tag{A.3}$$

$$\int \sin^2 x\,\mathrm{d}x = \frac{1}{2}x - \frac{1}{4}\sin 2x, \tag{A.4}$$

$$\int \sin^4 x\,\mathrm{d}x = \frac{3}{8}x - \frac{1}{4}\sin 2x + \frac{1}{32}\sin 4x. \tag{A.5}$$

Acknowledgement

This project was supported by the Royal Dutch Academy of Sciences and the Dutch Technology Foundation (grant STW EWO.5928).

References

Alart, P., Curnier, A., 1991. A mixed formulation for frictional contact problems prone to Newton like solution methods. Comput. Methods Appl. Mech. Engrg. 92, 353–375.

Anitescu, M., Potra, F.A., 1997. Formulating dynamic multi-rigid-body contact problems with friction as solvable linear complementarity problems. Nonlinear Dynamics 14 (3), 231–247.

Brogliato, B., 1999. Nonsmooth Mechanics, 2nd edition. Springer, London.

Bronstein, I.N., Semendjajew, K.A., 1984. Taschenbuch der Mathematik, 21st edition. Harri Deutsch, Thun.

Contensou, P., 1963. Couplage entre frottement de glissement et frottement de pivotement dans la théorie de la toupie. In: Ziegler, H. (Ed.), Kreiselprobleme und Gyrodynamics, IUTAM Symposium Celerina, 1962. Springer-Verlag, Berlin, pp. 201–216.

Friedl, C., 1997. Der Stehaufkreisel. Master's thesis. Universität Augsburg.

Glocker, Ch., 1995. Dynamik von Starrkörpersystemen mit Reibung und Stößen. Fortschr.-Ber. VDI. 18 (182).

Glocker, Ch., 1998. Formulation of spatial contact situations in rigid multibody systems. Comput. Methods Appl. Mech. Engrg. 177, 199–214.

Glocker, Ch., 2001. Set-Valued Force Laws, Dynamics of Non-Smooth Systems. In: Lecture Notes in Appl. Mech., Vol. 1. Springer-Verlag, Berlin.

Hairer, E., Wanner, G., 2002. Solving Ordinary Differential Equations II; Stiff and Differential-Algebraic Problems, 2nd edition. In: Springer Ser. Comput. Math., Vol. 14. Springer, Berlin.

Johnson, K.L., 1985. Contact Mechanics. Cambridge University Press, Cambridge.

Kuypers, F., 1990. Klassische Mechanik. VCH-Verlagsgesellschaft, Weinheim.

Laursen, T.A., Simo, J.C., 1993. Algorithmic symmetrization of Coulomb frictional problems using augmented Lagrangians. Comput. Methods Appl. Mech. Engrg. 108, 133–146.

Leine, R.I., Glocker, Ch., Van Campen, D.H., 2003. Nonlinear dynamics and modeling of various wooden toys with impact and friction. J. Vib. Control 9 (1), 25–78.

Magnus, K., 1971. Kreisel; Theorie und Anwendungen. Springer-Verlag, Berlin.

Moreau, J.J., 1988. Unilateral contact and dry friction in finite freedom dynamics. In: Moreau and Panagiotopoulos (1988), pp. 1–82.

Moreau, J.J., Panagiotopoulos, P.D. (Eds.), 1988. Non-Smooth Mechanics and Applications. In: CISM Courses and Lectures, Vol. 302. Springer, Wien.

Murty, K.G., 1988. Linear Complementarity, Linear and Nonlinear Programming. In: Sigma Series in Appl. Math., Vol. 3. Heldermann, Berlin.

Pfeiffer, F., Glocker, Ch., 1996. Multibody Dynamics with Unilateral Contacts. Wiley, New York.

Rockafellar, R.T., 1976. Augmented Lagrangians and applications of the proximal point algorithm in convex programming. Math. Oper. Res. 1 (2), 97–116.

Simo, J.C., Laursen, T.A., 1992. An Augmented Lagrangian treatment of contact problems involving friction. Comput. & Structures 42 (1), 97–116.

Stewart, D.E., Trinkle, J.C., 1996. An implicit time-stepping scheme for rigid body dynamics with inelastic collisions and Coulomb friction. Int. J. Numer. Methods Engrg. 39 (15), 2673–2691.

Stiegelmeyr, A., 2001. Zur numerischen Berechnung strukturvarianter Mehrkörpersysteme. Fortschr.-Ber. VDI. 18 (271).

Zhuravlev, V.G., 1998. The model of dry friction in the problem of the rolling of rigid bodies. J. Appl. Math. Mech. 62 (5), 705–710.